

**UPPER CRUSTAL STRUCTURE ACROSS THE EASTERN LAU SPREADING CENTER USING  
P-TO-S CONVERTED SEISMIC WAVES**

A THESIS SUBMITTED TO THE GRADUATE DIVISION OF THE UNIVERSITY OF HAWAII AT  
MĀNOA IN PARTIAL FULFILLMENT OF THE REQUIREMENTS FOR THE DEGREE OF

**MASTER OF SCIENCE**  
**IN**  
**EARTH AND PLANETARY SCIENCES**

DECEMBER 2019

By  
**CHARU LATA**

Thesis Committee:

Robert Dunn, Chairperson

Deborah Eason

Neil Frazer

Rhett Butler

**Keywords:** Lau back-arc basin; Eastern Lau Spreading Center (ELSC), Oceanic upper crust; Shear waves;  
Controlled source seismology

## **Acknowledgements**

I would like to thank my advisor and committee chair, Robert Dunn, for his invaluable expertise, guidance, and encouragement over the past years, as well as for securing the funding for this research. I would like to thank my committee members, Deborah Eason, Neil Frazer and Rhett Butler, for their insights and advice. I am thankful to the administrative staff of the University of Hawai‘i at Mānoa, Department of Earth Sciences – particularly Lily Shao and Susan Van Gorder – for all of their help. I am thankful to the Captain, crew and science team of survey MGL0903, the data of which is used in this study. Finally, I would like to thank my family and friends for their love and support throughout this project.

This research is funded under National Science Foundation grant OCE16-34460

## Abstract

Located alongside the active Tofua Arc within the Lau backarc basin, the Eastern Lau Spreading Center (ELSC) appears to generate two types of oceanic crust. Crust formed near the active arc, where the mantle is thought to contain relatively high amounts of slab-derived water, is abnormally thick (8-9 km) and compositionally stratified with relatively evolved lavas and an unusually mafic lower crust. Farther from the arc, where water contents are expected to be lower, the crustal structure is more typical of crust formed at intermediate-to-fast-spreading mid-ocean ridges, and lava samples are dominantly basaltic. In this study, P and S wave data from the L-SCAN active-source wide-angle reflection/refraction experiment are modelled to place additional constraints on upper crustal structure. A combination of ray tracing and finite difference numerical wavefield simulation is used to identify P and P-to-S converted seismic phases. The phases primarily arise from two shallow interfaces, one at only ~80 m depth or less, and the other at 500-650 m depth. The shallower interface is deeper than the sediment base, is observed all across the study area, and is interpreted as a 'layer 2Aa' boundary, proposed to result from a step change in crustal porosity. The deeper interface is interpreted as the layer 2A-2B boundary, corresponding to a transition from lavas to sheeted dykes. Layer 2A, on average, is 150 m thicker in crust that formed at the spreading center when spreading was located near the arc, as compared to when spreading was located farther away from the arc. Layer 2A thickness and  $V_p/V_s$  values indicate that a thicker and porous lava layer, dominated by basalts to basalt-andesites, cap near-arc crust, while a thinner and less-porous, mostly basaltic, volcanic layer caps the far-arc crust. These results are consistent with the waning influence of slab-derived volatiles on crustal formation as spreading moves away from the active arc.

## Table of Contents

Acknowledgements.....	ii
Abstract.....	iii
Table of Contents.....	iv
Table of Figures.....	v
List of Tables.....	vi
1. Introduction.....	1
2. Study Area.....	2
2.1 Crustal Domains.....	3
2.2 Upper Oceanic Crustal Layer 2A.....	4
3. Experiment Layout and Data Processing.....	5
4. Observations.....	6
5. Methods and Preliminary Results.....	9
5.1 Near-range Data.....	10
5.2 Far-range Data.....	15
6. Results.....	17
7. Discussion.....	22
7.1 Near Surface Layer.....	22
7.2 Layer 2A.....	23
7.3 Subduction Influence on Upper Crustal Structure.....	24
8. Conclusions.....	25
References.....	26
Appendix A.....	33
Appendix B.....	38
Appendix C.....	40
Appendix D.....	42
Appendix E.....	44

## Table of Figures

Figure 1. Bathymetry map of the study area and layout of the L-SCAN experiment. ....	3
Figure 2. Schematic ray diagram showing wave phase conversion. ....	6
Figure 3. Common receiver gathers, out to 10 km range, of the vertical (Z) and radial (R) components for three receivers. ....	7
Figure 4. Common receiver gathers of the L and Q components of three receivers out to 30 km range. ....	9
Figure 5. Synthetic travel times versus range for the same source-receiver geometry in Figure 3. ....	10
Figure 6. Zoepritz solutions for a downgoing wave. ....	11
Figure 7. Numerically simulated elastic wavefields and seismic source gathers within 10 km range from receiver for the same 2 models in Figure 6. ....	14
Figure 8. Zoepritz solutions for an upgoing wave. ....	15
Figure 9. Zoepritz solutions for an upgoing wave and its multiples. ....	16
Figure 10. Sonar image of the study area and observed SS traveltimes for each station. ....	19
Figure 11. Reflector depths (in m) beneath a station versus a station's distance to the ridge axis for the different crustal domains ....	20
Figure 12. Layer 2A estimated thicknesses (a) and $V_p/V_s$ values (b) overlain on a map view tomographic slice of upper crustal P-wave velocities (from Dunn et al., 2013). ....	21
Figure 13. Scatter plot of layer 2A thickness (in km) versus $V_p/V_s$ across the study area, highlighting differences between the crustal domains. ....	22
Figure 14. Cartoon interpretation of sediment layer and upper crustal structure as a function of arc proximity. ....	25
Figure A1. Source receiver geometry used for component orientation calculation. ....	33
Figure A2. Example of common receiver gather recorded in the three components of geophone for the source receiver geometry in Figure A1. ....	34
Figure B1. Data processing flow chart. ....	38
Figure B2. Cartoon showing component rotation. ....	38
Figure C1. Staggered gridding used for numerical calculation of elastic wave propagation in isotropic media for a fourth-order scheme in space (After Thorbecke and Draganov, 2012). ....	41

**List of Tables**

Table D1. Near surface shear wave velocities and layer thicknesses..... 42

Table E1. Layer 2A shear wave velocities and layer thicknesses..... 44

## 1. Introduction

Oceanic crust formed along intermediate-to-fast spreading-rate mid-ocean ridges is often considered to have, on average, a simple vertical structure. From the top, the sequence first consists of a shallow crustal layer of a few hundred meters thickness characterized by low seismic velocities (<5 km/s P-wave velocity) and high seismic attenuation, the lower boundary of which is marked by a strong velocity gradient that can be imaged with seismic reflection techniques (e.g., Harding et al., 1993; Vera and Diebold, 1994; Wilcock et al., 1995; Detrick et al., 1998). Known as seismic layer 2A, it is often interpreted in terms of a lithology composed of high-porosity extrusive basalts, based on analogy with ophiolite units (subaerial exposures of oceanic and back-arc crust) (e.g., Coleman, 1977; Nicolas, 1989; Dilek and Furnes, 2011), the seismic velocity of laboratory samples of dredged and drilled rocks, in situ measurements in drill holes (e.g., Detrick et al., 1994; Karson 1998), and observations within “tectonic windows” into oceanic crust, such as Hess Deep (Karson et al., 2002). By further analogy to ophiolites and other observations, seismic layer 2A is underlain by a higher-velocity region, with a lower seismic gradient, of sheeted dikes (seismic layer 2B; 4.5-6 km/s P-wave velocity), followed by an even higher-velocity region of gabbros (layer 3; 6.5-7 km/s P-wave velocity). These three layers together form the crustal assembly, which is generally 6-7 km thick (White et al., 1992). This simple model has served for many years to provide a framework for broader investigation and comparisons, but it is now known that ocean crust varies strongly from setting to setting, and does not always conform to these expectations (e.g., Livermore et al., 1997; Martinez and Taylor 2002; Becker et al., 2010).

While spreading rate is a dominant factor that controls crustal structure along mid-ocean ridges (Reid and Jackson, 1981; Parmentier and Phipps, 1990), in back-arc settings slab-derived volatiles, principally water, appear to influence melting processes and crustal formation, overprinting spreading-rate trends (Martinez and Taylor, 2002; Eason and Dunn, 2015). The presence of water during melting is expected to enhance melt production (e.g., Davies and Bickle, 1991; Stolper and Newman, 1994), with the water ending up in the melt (e.g., Hirth and Kohlstedt, 1996). The presence of water may also lead to more silicic lavas on average (e.g., Nicholls and Ringwood, 1973; Sisson and Grove, 1992; Gaetani and Grove, 1994; Eason and Dunn, 2015). One major observation is that when a back-arc spreading ridge is located close to an active arc system, the magma supply to the ridge appears to be relatively high, with a corresponding thicker upper crust and thicker total crust (Martinez and Taylor, 2002; Dunn and Martinez 2011; Arai and Dunn 2014), and lavas erupted at the ridge have higher water contents, with compositions ranging from basalts, to andesites, to rhyolites (e.g., Jenner et al., 1984; Tamura et al., 2008).

Along the active Eastern Lau Spreading Center (ELSC) in the Lau back-arc basin, studies have revealed systematic variations in crustal structure formed at the spreading center as a function of distance to the volcanic arc. For example, as the axis of the spreading center approaches the arc to the south, seismic layer 2A is observed to thicken, while the average P-wave velocity of layer 2A decreases (Jacobs et al., 2007). More generally across the Lau basin, geophysical studies reveal that crust formed near the Tofua Arc is abnormally thick (8–9 km) and compositionally stratified, with a thick low-velocity upper crust and an abnormally high-velocity lower crust (Arai and Dunn, 2014). Lava samples from this area have arc-like compositional enrichments and tend to be more vesicular and

differentiated than typical mid-ocean ridge basalts (Pearce et al., 1994; Escrig et al., 2009). It has been proposed that slab-derived water entrained in the near-arc ridge system not only enhances mantle melting, but also affects magmatic differentiation and crustal accretion processes (Eason and Dunn, 2015).

With a rough association between seismic layer 2A and extrusive basalts, one could map out variations in layer 2A thickness and wave speed to better understand variations across these crustal domains with respect to extrusive layer properties. Upper crustal interfaces such as the base of a sediment layer and base of layer 2A are strong first order seismic discontinuities that may cause compressional seismic phases (P waves) to convert to shear phases (S waves) (e.g., White and Stephen, 1980; Christensen et al 1997; Eccles et al., 2009). Such phase converted arrivals were strongly and consistently recorded on 3-component ocean-bottom seismographs located across the Lau basin during the L-SCAN active-source seismic experiment (**Figure 1**; Dunn et al., 2013). This experiment consisted of a large two-dimensional array of seismographs and dense airgun-source seismic lines centered on the Eastern Lau Spreading Center. The data provide an opportunity to study upper crustal shear wave structure across the backarc region as a function of distance from the active arc and the subducting slab's influence on crustal processes.

## **2. Study Area**

The Eastern Lau Spreading Center (ELSC) is located within the Lau Basin (**Figure 1A inset**), which is a wedge-shaped back-arc basin bordered by the Lau Ridge remnant arc to the west and the currently active Tofua arc to the east (Karig, 1970; Hawkins, 1995). The basin is proposed to have opened ~6 My ago (Hawkins, 1994) as a result of arc rifting and crustal extension. The basin opening was accommodated by regions of localized seafloor spreading, along with more diffuse spreading and magmatic intrusion, giving rise to an uneven and discontinuous seafloor (Taylor et al., 1996; Austin et al., 2012). Between 2–4 My, crustal extension was dominated by the southward propagation of seafloor spreading (Parson et al., 1990; Hawkins et al., 1994; Taylor et al., 1996), which continues today along the Central Lau Spreading Center (CLSC), ELSC and Valu Fa Ridge (VFR). Along these spreading centers, the spreading rate decreases from north to south: from ~90 mm/yr in the north at the CLSC, to ~60 mm/yr at the southern ELSC, to ~40 mm/yr at the VFR (Taylor et al., 1996, Zellmer and Taylor, 2001).

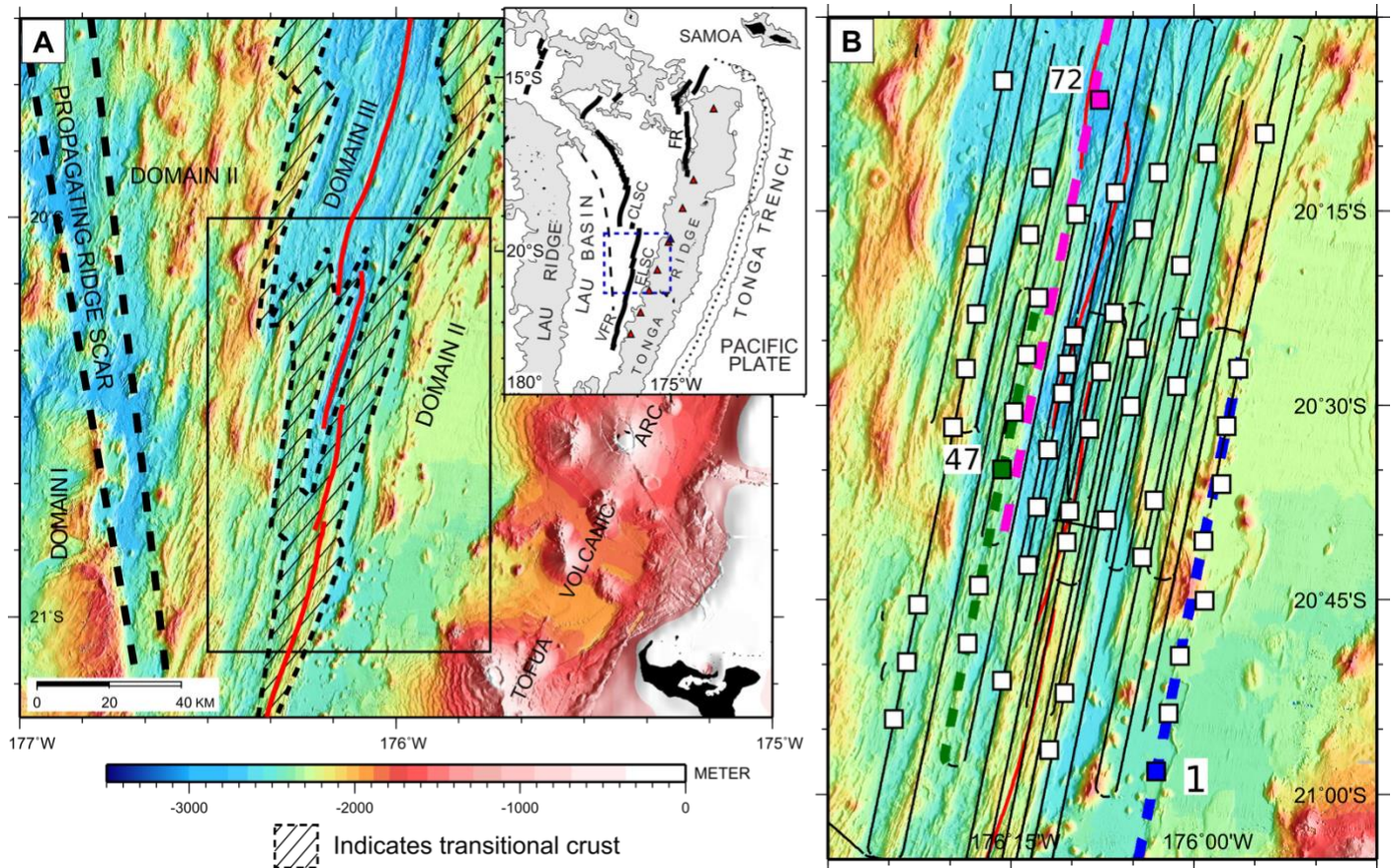


**Figure 1.** Bathymetry map of the study area and layout of the L-SCAN experiment. Panel (a) shows a bathymetry map overlain by dashed lines and labels to indicate the crustal domains, as described in **Section 2.1**. The inset shows the overall location of the study area. The black box indicates the area shown in (b). Panel (b) shows locations of ocean bottom seismographs (white squares) and the subset of seismic source lines (black lines) used in this study. The colored OBS and colored dashed lines (shown in blue, magenta, and green) refer to instruments and source lines discussed in **Section 4**, and shown in **Figures 3** and **4**. Figure modified from Dunn et al. (2013).

## 2.1 Crustal Domains

Along mid-ocean ridges, as the spreading rate decreases the melt flux due to passive upwelling decreases, and the ridge axis is expected to transform from an axial high region, bounded by faults with relatively small throws, to an axial valley, bounded by faults with large throws (e.g., Small and Sandwell, 1989; Lin and Morgan, 1992; Morgan and Ghen 1993). However, along the ELSC opposite trends are observed. From north to south, as the spreading rate decreases the ELSC moves ~40 km closer to the active Tofua Arc. As this happens, the ridge morphology changes from a more faulted and deep rifted valley to a less faulted and broad axial high. Furthermore, lava samples from the ridge axis show stronger enrichments in subduction-related components relative to typical mid-ocean ridge basalts in the south (Escrig et al., 2009; Bézoz et al., 2009). In addition, lava samples from the southern ELSC are more evolved (basaltic-andesites) and highly vesicular as compared to the northern ELSC (e.g., Jenner et al., 1987; Vallier et al., 1991; Pearce et al., 1994). Since this discovery, several studies have investigated the anomalous nature of crust formed

along the ridge axis. Martinez and Taylor (2002) identified large domains across the Lau basin composed of differences in bathymetric depth and seafloor morphology, Bouguer gravity, rock chemistry, and other properties. They proposed that arc proximity overrides spreading rate controls on crustal formation. More recent seismic studies have also found corresponding changes in internal crustal structure as a function of arc proximity (Dunn and Martinez, 2011; Dunn et al., 2013; Arai and Dunn, 2014). Basin crust that was produced when the ridge was close to the arc is thicker and unusually stratified, with a thick low-velocity (3.4-4.5 km/s) upper crust and an abnormally high-velocity (7.2-7.4+ km/s) lower crust (Dunn et al., 2013; Arai and Dunn, 2014). Due to symmetric spreading, the ridge axis has produced this type of crust on both sides of the spreading center, leading to large semi-symmetric domains of anomalous crustal properties across the basin (Domain II in **Figure 1a**; Domain I is the crust produced in the basin before the ELSC propagated southward into its present location). On the other hand, crust produced when the ridge was farther away from the arc is less anomalous, and has a similar thickness and velocity structure as that formed at intermediate-spreading rate mid-ocean ridges (Domain III in **Figure 1a**).

The general consensus of these and other studies is that the change from anomalous crust to more typical crust is controlled by the waning influence of slab-derived volatiles on the magma supply as the ridge moves away from the arc. The mechanism of this influence, and processes that generate the unusual crustal stratification, was further studied by Eason and Dunn (2015). They proposed that slab-derived water entrained in the near-arc ridge system not only enhances mantle melting and crustal thickness, as commonly proposed to explain high crustal production in back-arc environments, but also affects magmatic differentiation and crustal accretion processes leading to the observed differences in lava composition and vertical crustal structure. In their model, slab-derived water in melts suppresses plagioclase crystallization and leads to the formation of an ultramafic lower crust, with higher seismic velocities, and a more felsic upper crust with unusually low seismic velocities, while successfully predicting major element compositional trends of the erupted lavas.

## **2.2 Upper Oceanic Crustal Layer 2A**

A few seismic studies have investigated the structure of seismic layer 2A along and across the ELSC. The most significant was published by Jacobs et al. (2007), which showed systematic variations in seismic layer 2A thickness and interval velocities along the ridge crest as a function of distance to the volcanic arc. Along the ELSC within our study area, the average thickness of layer 2A increases from 0.5 km to 0.62 km from north to south, while the average P-wave speed in layer 2A decreases from 3 km/s to 2.68 km/s, correlating with the change in lava composition from basalt to basaltic-andesite and with increased porosity. Results from this study, however, were limited to source lines located strictly along the axis of the spreading center.

A second and more recent seismic study was the L-SCAN active-source seismic tomography experiment (Dunn and Martinez, 2011; Dunn et al., 2013; Arai and Dunn, 2014; Dunn, 2015). The 70 x 120 km<sup>2</sup> study area was centered on the Eastern Lau Spreading Center and spanned crustal Domains II and III, and the narrow transition zone between them. Although the smooth tomography models prevent the identification of the base of layer 2A within acceptable limits for this study, the tomographic images show detailed lateral variations of seismic structure in the upper crustal

layers extending well away from the ridge. In particular, the upper 1 km of crust exhibits prominent domain-specific lateral variations in velocities, with average P-wave velocity of ~4 km/s in Domain II as compared to 5 km/s in Domain III. Furthermore, along the direction of spreading (perpendicular to the ridge axis) crustal domains exhibit step-like transitions in properties with as little as 5 km of incremental spreading, matching observed changes in seafloor depth and Bouguer gravity structure (Martinez and Taylor, 2002).

### 3. Experiment Layout and Data Processing

The L-SCAN seismic experiment (Dunn et al., 2013) consisted of 83 ocean bottom seismographs (OBS), each containing a hydrophone and a gimballed 3-component geophone, placed on the seafloor in a grid formation. The seismic source was the R/V Langseth's 36-element, 6600 in<sup>3</sup> airgun array towed at 9 m depth with sources located every 450–500 m. Fifty-seven dense source lines were carried out such that most OBSs were crossed by at least a ridge-perpendicular and a ridge-parallel pair of lines. See Dunn et al. (2013) for further details.

In this study, data processing steps included removing the instrument response from each channel, rotation of data components to increase the relative amplitudes of P-waves and S-wave in two principal directions with respect to each shot, frequency filtering, and a small amount of amplitude correction to adjust for geometric and intrinsic attenuation with increasing shot-to-receiver range. Because the in situ orientation of the horizontal components of the sensor was not known, water wave polarisation analysis was used to estimate them. The direct water wave first breaks were picked on record sections of the hydrophone channel, and then a 0.1 s time window after each pick was used to extract particle motions on the geophone channels. The geophone horizontal component orientation was then calculated by maximizing the radial energy as compared to the transverse energy, while maintaining positive polarity of the water wave on the radial component (e.g. Bratt and Solomon 1984; Anderson et al., 1987). Given the density of source lines around any one station, nearly complete azimuthal coverage for most stations was available, and orientation uncertainties were  $\leq 5^\circ$ . Out of 83 instruments, 50 were selected for this study (**Figure 1b**). The remaining instruments were discarded due to one or more inoperative components, component gain issues, poor signal-to-noise ratio, and/or intermittent ~6 Hz instrument noise issues. A complete listing is given in **Appendix A**.

Since wide-angle crustal P-wave refractions that arrive at non-vertical angles below the seafloor appear on radial records, for certain record sections we minimised this energy by performing another component rotation about the transverse axis to rotate Z-R to L-Q components (**Figure 2b**). This was done to increase the relative amplitude of P waves on the L component and S waves on the Q component (description given in **Appendix B**), mainly for far-offset data. However, due to scattering, dipping layers, and other non-2-D effects, the isolation of the P and vertically-polarized S waves (SV) was approximate. In our analysis we only used ridge-parallel source lines to avoid directional effects on wave speed and travel time, since the upper 1 km of crust is known to have ~3% anisotropy with the fast axis oriented parallel the ridge (Dunn, 2015).

#### 4. Observations

In an oceanic environment, P-to-S wave conversions can occur at sharp structural boundaries such as the seafloor and upper crustal layers, either along the downgoing ray path or the upgoing path beneath the receiver. **Figure 2** schematically depicts example phase conversions, which are just a few of several possibilities. Those shown, as discussed below, are dominant in seismic record sections in this environment. S waves can be identified by their unique orientations and slower travel times than P waves. However, the S waves may be coincident in time with P wave multiples, especially reverberations in the upper crustal or sediment layers, and because the P and P-to-S converted waves may have differing ray parameters, the S wave may appear on data records rotated to show P waves alone. Therefore, further distinguishing characteristics of S waves can be the nature of their traveltim moveout and amplitude variation with range.

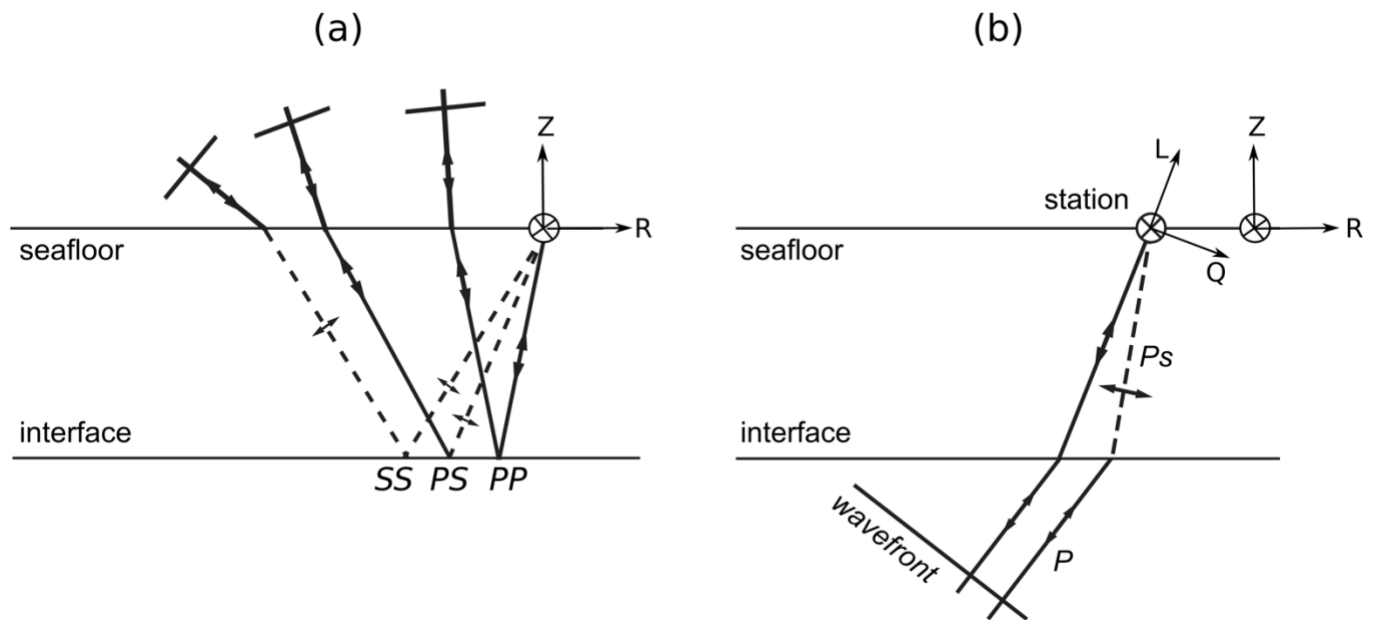


**Figure 2.** Schematic ray diagram showing wave phase conversion. **(a)** A water wave incident on the seafloor with phase conversion at the seafloor and at a reflecting interface below the station. PP is transmitted and reflected as a P-wave, PS is transmitted as a P-wave and reflected as a S-wave, and SS is transmitted and reflected as a S-wave. **(b)** An upgoing refracted P-wave below the station with a P-to-S conversion at an interface below the station, is called a Ps wave. The orientation of rotated instrument components about the transverse axis is also shown.

Several phase converted arrivals were identified in data recorded across the entire compliment of the 50 receivers. **Figure 3** shows examples of common-receiver-gather record sections, to 10 km range, for three receivers located within the different crustal domains (Z and R data components). The source line and receiver locations are shown in **Figure 1b**. Within the first 2 km, the first waves to arrive are the water waves; their arrival times at all ranges are marked in blue. At ranges greater than a few hundred meters, the water wave appears on both the vertical and radial components due to oblique arrival at the seafloor. Behind the water wave arrival, at larger travel times,

additional arrivals are clearly observed at sites 47 and 1 located 11 km and 20 km from the ridge crest (in the transition zone and Domain II), respectively. These nearly ‘water-wave parallel’ arrivals could be reflected PP, SS, or PS converted waves from the base of a sediment or upper crustal layer (**Figure 2a**), or multiples within layers. **Section 4** describes how the different phases were identified.

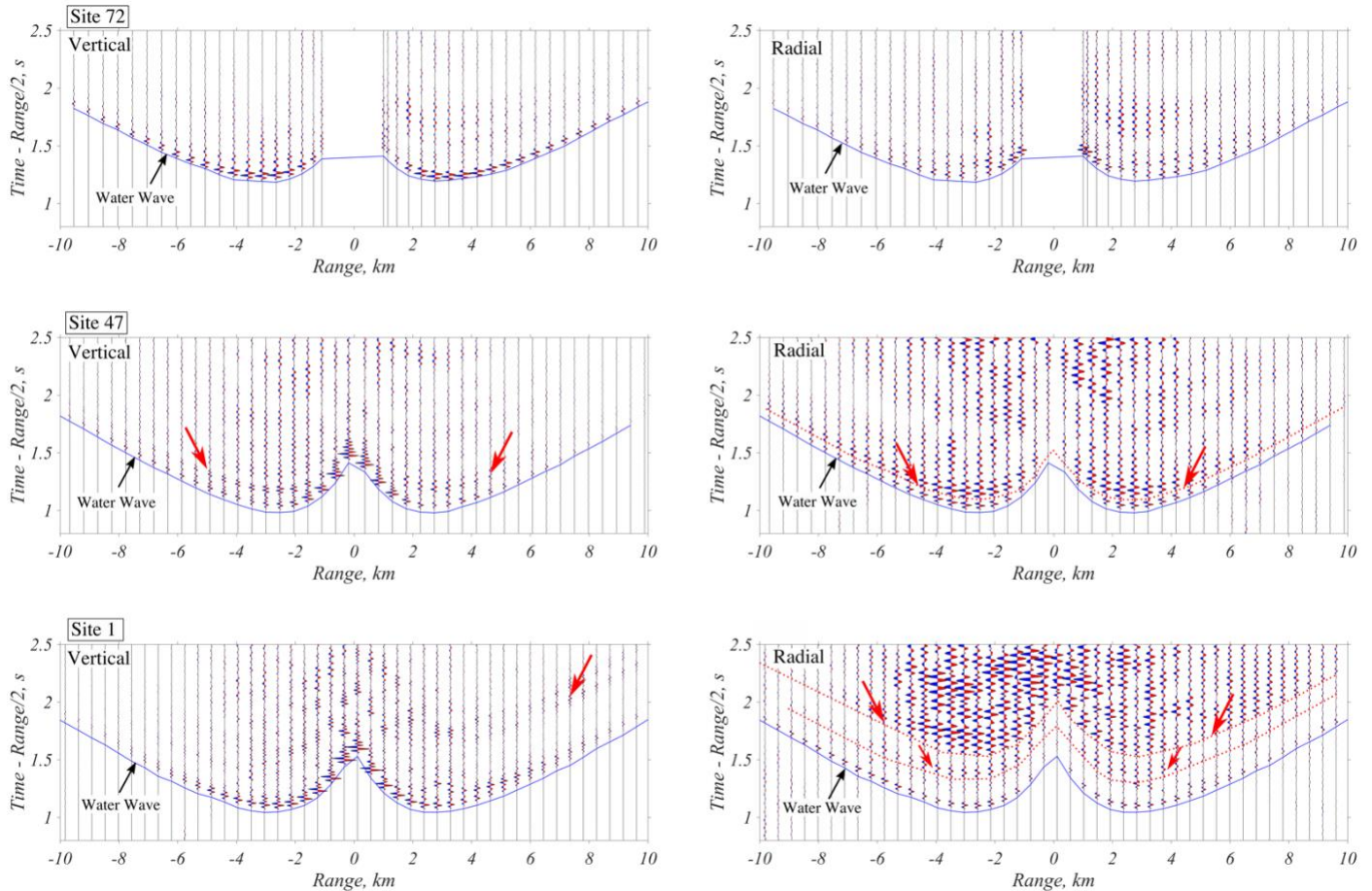


**Figure 3.** Common receiver gathers, out to 10 km range, of the vertical (Z) and radial (R) components for three receivers. The corresponding source lines and receiver locations are given in **Figure 1b**. **(Top row)** A station located 2 km from the axis of the spreading center within Domain III. **(Middle Row)** A station located 11 km from the axis of the spreading center in the transition zone. **(Bottom Row)** A station located 20 km from the axis of the spreading center within Domain II. The water wave arrivals (blue line) and shear waves (red arrows) are marked in each plot. The data were bandpass filtered 15–35 Hz (Butterworth filter with 24 dB/octave attenuation roll off) and are amplitude adjusted by a factor of  $(1+r)^{1.2}$  where  $r$  is the source-to-receiver range.

At shot ranges of ~2 to 30 km, seismic phases arriving before the water wave have travelled deeper into the crust. **Figure 4**, shows these deeper arrivals for the same stations in **Figure 3**. Here L and Q component records are plotted rather than Z and R (as in **Figure 3**) to isolate the P and S arrivals. These include crustal P-wave refractions from layers 2 and 3 that appear strongly on the L component. Layer 2 P-wave refractions are detected at 2-10 km

range, with apparent speeds of 4-5 km/s and arrive at the station with estimated incidence angles between 10°-15° (on the basis of wave polarizations). Layer 3 P-wave refractions are detected at 8-30 km range with apparent speeds of 6.8-7.4 km/s and arrive at the station with estimated incidence angles of less than 10°. Recorded on the Q component, and closely following the crustal P refraction, are P-to-S converted waves (Ps). The Ps arrivals have similar apparent velocities as the pre-arriving P phase, which indicates that the P-to-S conversion occurs beneath the receiver (**Figure 2b**). This conversion could occur at the strong upper crustal seismic discontinuities such as the sediment base or deeper at a layer 2A-2B boundary, within the igneous crust. Also arriving behind the Ps phase and closely following the Ps or P traveltimes curve, are shear wave reverberated arrivals. These reverberations occur within the upper crustal layers, due to their near-parallel nature of traveltimes with respect to the P or Ps phase. The Ps and its multiples were not consistently observed on both sides of the receiver, possibly indicating source side scattering effects or local variations in structure beneath a receiver.

The mean travel time difference between the P and Ps phases at each station is observed to spatially vary across the crustal domains (**Figure 4**). The receiver at site 72, located in Domain III and 2 km away from the ridge axis, exhibits a Ps versus P travel time difference of ~0.15 s. While receiver at site 47, located in the transition zone and 11 km from the ridge axis, recorded a delay of ~0.6 s. The greatest difference, ~0.8 s, was observed at site 1, located in Domain II and 20 km away from the ridge axis. The travel time delays correlate positively with the distance of a receiver from the ridge axis. Since, in general, sediment thickness correlates positively with distance from the ridge axis, one possibility would be that the observed S-wave arrivals are produced as a result of phase conversion of P to S at the base of sediments. To understand whether all or only part of the delay time is caused by a sediment layer, we use the near range data (e.g., **Figure 3**) to extract a near surface delay. Once the near surface delays are removed from the overall delay times at longer ranges, we interpret the corrected delay times and obtain the interface depth of the phase conversion and S-wave speeds.

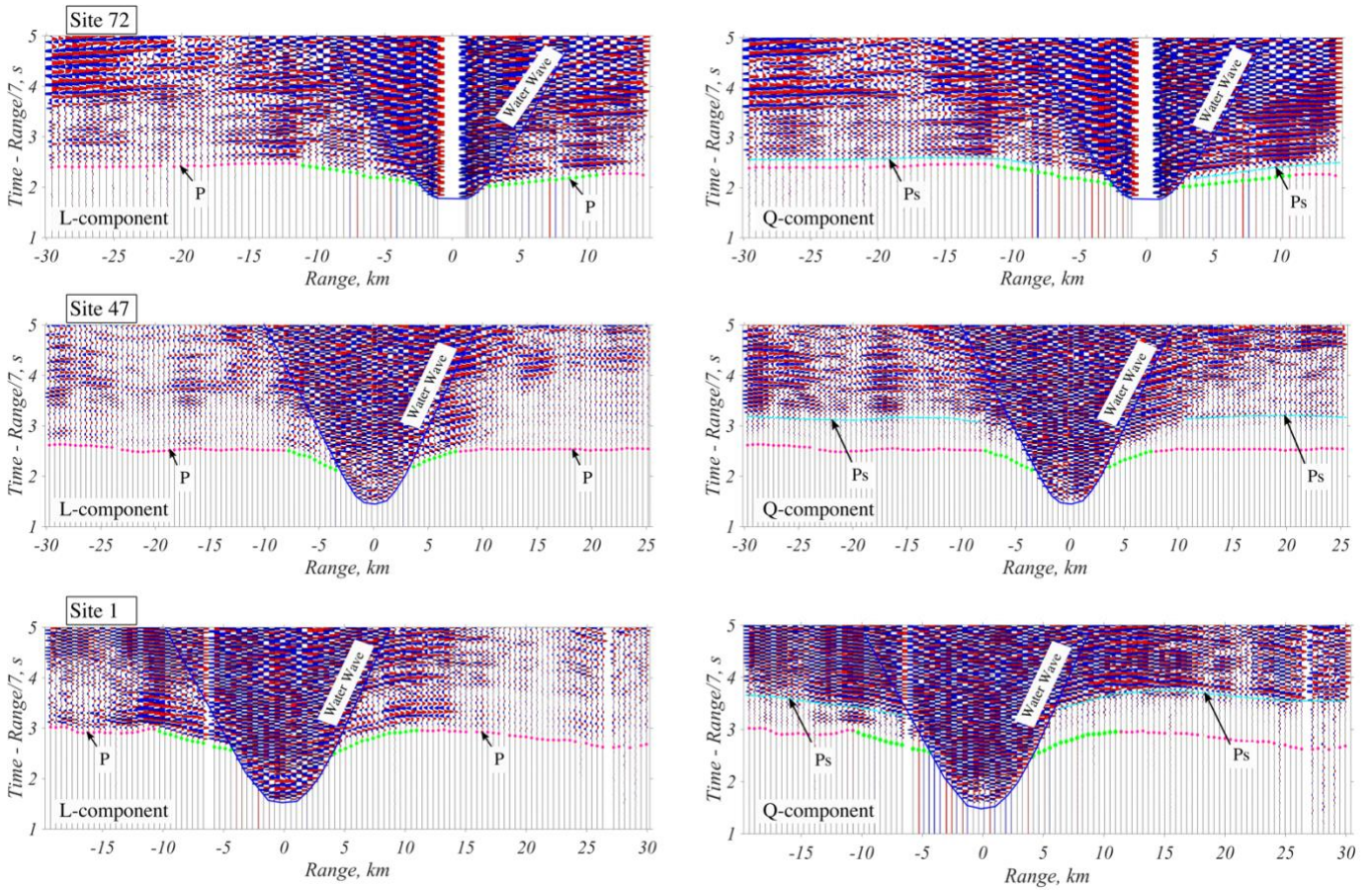


**Figure 4.** Common receiver gathers of the L and Q components of three receivers out to 30 km range. From top to bottom, these are the same receivers shown in **Figure 3**. Upper crustal (green dots) and lower crustal (pink dots) P-wave refractions are strongly observed on the L component. For reference, these arrivals are also indicated on the Q-component records. The water wave arrivals are indicated by a blue line. The records are displayed with a reduction speed of 7 km/s, so that lower crustal refractions and their multiples appear approximately horizontal. The data were bandpass filtered 2 - 15 Hz (Butterworth filter with 24 dB/octave attenuation roll off) and are amplitude-adjusted by a factor of  $(1+r)^{1.2}$  where  $r$  is the source-to-receiver range.

## 5. Methods and Preliminary Results

The observations show a variety of P and S wave arrivals at near and far ranges. To identify these arrivals, we examined wave amplitudes and polarizations as a function of range using comparison with synthetic results, discussed in **Sections 5.1 and 5.2**. In Section 5.1, we first compared two velocity models which could reproduce the traveltimes of observed shear waves in the near range data. Then we modelled the partitioning of the water wave at the seafloor into downgoing P and S waves to investigate the conversion efficiency at the seafloor as a function of ray parameter, by using solutions to the Zoeppritz equations (Zoeppritz, 1919; Aki and Richards, 2002). Next we modelled the wavefield for a simple layered structure to understand P and S wave amplitudes, polarizations, and traveltimes of the phases arriving behind the water wave. The insights gained from synthetic modelling was used to identify and pick the

P and S wave first breaks in the observed data. By reducing the misfit between observed traveltimes and predicted traveltimes, derived from ray tracing (Margrave, 2001), we calculated the average S-wave velocity and layer thickness of the top-most resolvable seismic layer beneath the seafloor. Using these near-surface values for velocity and layer thicknesses, we calculated the P-to-S delay caused by this layer for an upgoing wide-angle deep crustal refraction. We found that calculated delays for the upgoing P-to-S converted wave at the modelled interface were not able to explain the observed P-to-S delays. Hence, the observed wide-angle Ps waves are expected to have converted at a deeper interface not readily observed by the near-offset data processing. In **section 5.2**, we show results from synthetic modelling of amplitudes of converted shear waves as a function of ray parameter using Zoeppritz equations. This was used to identify the nature of observed shear waves. Once identified, their travel times were used to obtain estimates of associated layer depths and velocities (after correction for the near-surface P-to-S delay).

### 5.1 Near-range Data

Preliminary traveltimes modelling of the shear waves in the near range data (red arrows in **Figure 3**) indicated that these high-amplitude arrivals, with traveltimes closely following the water wave at ranges up to 10 km, are of either PS or SS type (**Figure 2a**). Here we show two possibilities. In one model, we mimic a sedimented seafloor with a 40 m thick low-velocity layer ( $V_p = 1.58$  km/s,  $V_s = 0.3$  km/s) overlying a higher-velocity crustal layer. The second model mimics an un-sedimented seafloor with a shallow 110 m thick low-velocity crustal layer ( $V_p = 2.2$  km/s,  $V_s = 0.7$  km/s). While the PS and SS phases in the first model replicate the observed travel times of the shear waves (**Figure 5a**), the SS phase in the second model also reproduces the travel times (**Figure 5b**). Hence we need further distinguishing information such as P-to-S conversion amplitudes for the two models.

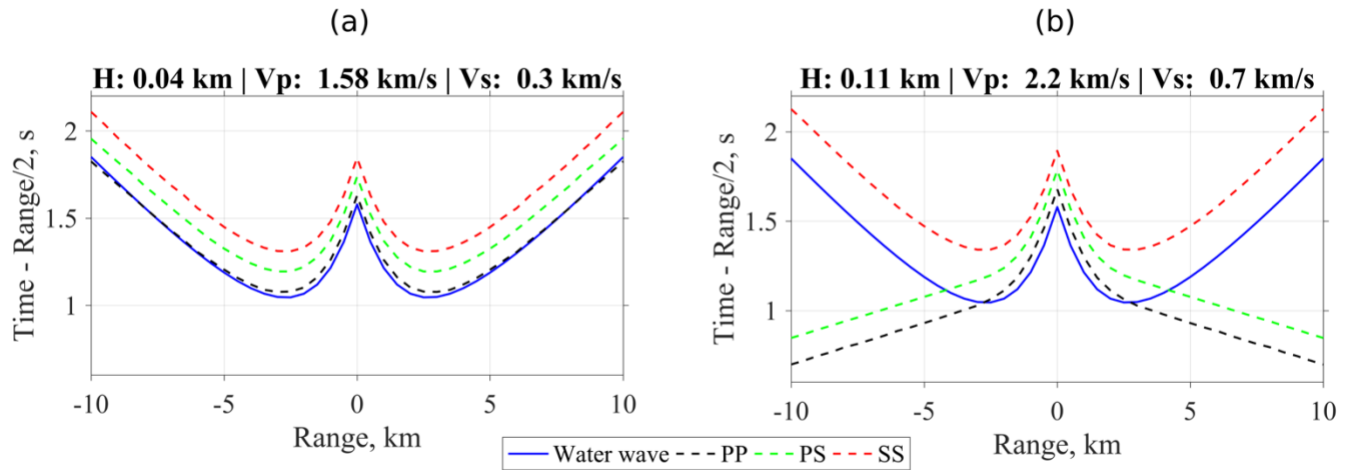


**Figure 5.** Synthetic travel times versus range for the same source-receiver geometry in **Figure 3**. (a) For a low velocity seafloor and (b) for a high velocity seafloor. Medium properties are titled in each figure. The phases PP, PS and SS are defined in **Figure 2**.

For these two models, solutions to the Zoeppritz equations were used to estimate variations in amplitude of P and SV phases with source-receiver range (and ray parameter) for an incident water wave at the seafloor. Density was

determined from the relation  $\rho = 1.85 + 0.165Vp$  (Christeson and Shaw, 1970). For a downgoing water wave, **Figure 6** shows the efficiency of P-to-S conversions for the two seafloor types. For a low-velocity seafloor, the transmitted P wave (dashed blue line) has an amplitude that is  $\sim 60\%$  of the incident wave within the critical angle of incidence, as opposed to  $\sim 40\%$  for a high-velocity seafloor (solid blue line). Critical incidence, defined by  $90^\circ$  refraction angle ( $= \sin^{-1}(Vp_w / Vp_1)$ ), is marked by a local drop in S amplitude and a jump in P wave amplitude. Due to the inverse relation of critical angle with seafloor velocity, the critical incidence is reached at a smaller angle (smaller ray parameter) and hence at a shorter range for a high-velocity seafloor as compared to a low-velocity seafloor. Conversion from P-wave phase to S-wave phase is observed to increase with the angle of incidence of water waves in both cases, with a  $\sim 50\%$  lower amplitude coefficient for the low-velocity seafloor. The amplitude of converted waves increases post critical incidence, with stronger conversion for high-velocity seafloor. In summary, a high-velocity seafloor produces a relatively strong down-going P-to-S conversion for post-critical incidence (roughly 2.7 km range in 3 km of water), while a low velocity seafloor produces a weak conversion at all ranges. Considering that the water-sediment interface may have even more gradual increase in properties than modelled here, it is likely that a sedimented seafloor does not produce a strong P-to-S conversion of the downgoing water wave.

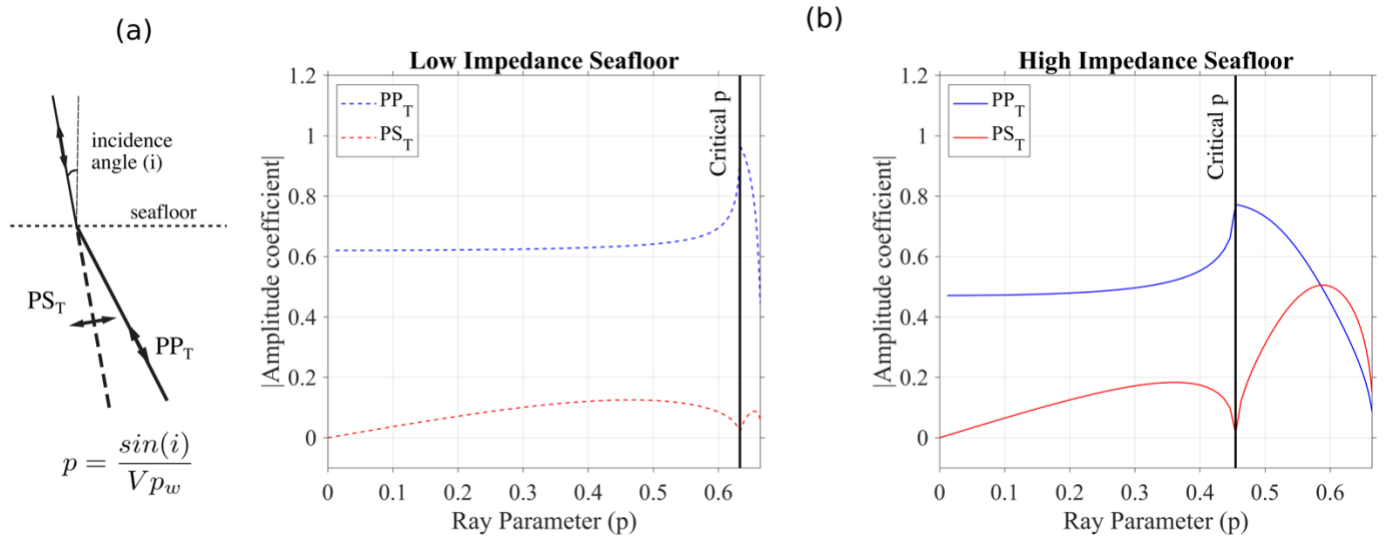


**Figure 6.** Zoeppritz solutions for a downgoing wave. **(a)** Schematic ray diagram representing P-to-S conversion of a downgoing water wave at the seafloor for a specific ray parameter,  $p$ , related to incidence angle by the given equation. **(b)** Relative amplitude of  $PP_T$  (blue) and  $PS_T$  (red) with respect to the water wave, as a function of ray parameter, for the two cases discussed in the text. Both cases have a water layer ( $Vp_w = 1.5$  km/s,  $Vs_w = 0$  km/s,  $\rho_w = 1000$  kg/m<sup>3</sup>), underlain by a halfspace (dashed lines on left corresponds to case with a low impedance contrast,  $Vp_1 = 1.58$  km/s,  $Vs_1 = 0.3$  km/s,  $\rho_1 = 2100$  kg/m<sup>3</sup>, and solid lines on right correspond to a higher impedance contrast,  $Vp_1 = 2.2$  km/s,  $Vs_1 = 0.7$  km/s,  $\rho_1 = 2300$  kg/m<sup>3</sup>). In both the cases, the vertical lines (solid or dashed) represents the ray parameter at critical incidence.

To further understand the traveltimes of different phase converted waves and their amplitude variations with range as a function of seafloor type, we simulated waves from a point source travelling in a layered velocity model. We used a finite difference numerical solution to the stress-velocity coupled wave equation (Levander 1988), to model phase converted reflections from an interface below the seafloor. A detailed explanation and code can be found in **Appendix C**. The 1-D model (**Figure 7h, 7i**) consisted of a 2400 m thick water layer, a 1-km-thick upper crustal layer, and a lower halfspace. The time and space steps were set to 0.001 s and 0.03 km respectively. In the first case, the velocities and density of the layer are ( $V_{p1} = 1.58$  km/s,  $V_{s1} = 0.3$  km/s,  $\rho_1 = 2100$  kg/m<sup>3</sup>) and the lower halfspace are set to  $V_{p2} = 3$  km/s,  $V_{s2} = 1$  km/s,  $\rho_2 = 2400$  kg/m<sup>3</sup> (**Figure 7h**) to mimic a sediment to layer 2A transition. In the second case, the velocities and density of the layer are ( $V_{p1} = 2.6$  km/s,  $V_{s1} = 1$  km/s,  $\rho_1 = 2300$  kg/m<sup>3</sup>) and the lower halfspace are set to  $V_{p2} = 4$  km/s,  $V_{s2} = 2$  km/s,  $\rho_2 = 2500$  kg/m<sup>3</sup> (**Figure 7i**) to mimic a layer 2A-2B transition. The point source is located at sea surface and the receivers are located on the seafloor with 500 m interval spacing, which record an elastic wave's particle velocities in the vertical and radial directions.

For the case of a low-velocity seafloor, the water wave conversion into the subsurface as an S-wave is minimal (as previously observed using the Zoeppritz equations' solutions), and a stronger transmitted P-wave is observed (**Figure 7a, 7b**). The transmitted P-wave is then reflected back more strongly from the subsurface interface as a P-wave (labelled  $PP_R$ ), as compared to a reflected S-wave (labelled  $PS_R$ ). Note that due to the difference in propagation direction, the  $PP_R$  phase is recorded with reversed polarisation with respect to water wave on the vertical component (**Figure 7g**). As the waves propagate, multiples of the P-wave within the sediment layer are observed ( $PPP_R$ ) with little to no conversion from P to S at lower boundary. An additional observation is that a strong downgoing transmitted S-wave is observed at the base of the sediment layer in the wavefield simulation, which would be important to creating S-S reflections from deeper layers not included in this simulation, for example.

In the second case, with high-velocity seafloor, the water wave efficiently transmits into the subsurface as an S-wave at oblique incidence (**Figure 7d, 7e**). This S-wave gets reflected from the subsurface interface and is recorded at the station ( $SS_R$ ) on both vertical and radial components (being relatively stronger in the radial direction). The amplitude of  $SS_R$  is low to zero at ranges within critical values ( $<2.5$  km), and it increases at ranges  $>2.5$  km. The wave polarisations of  $SS_R$  is found to be the same as that of the water wave in the radial direction. The second prominent wave recorded by the receivers is the  $PP_R$  arrival, which is recorded stronger on the vertical component and with reversed polarisation with respect to the water wave. The polarisation and amplitude variation with range of  $SS_R$  and  $PP_R$  phases were instrumental in identifying the arrivals in the real data. In all cases, ray tracing was able to predict the arrival times of each of the different observed phases, shown by the labelled lines in **Figure 7g, 7i**.

While ray tracing indicated that the observed shear waves can be of  $PS_R$  kind, numerical modelling has shown that the  $PS_R$  wave has a very low amplitude as compared to an  $SS_R$  wave. Since high amplitude shear waves are observed consistently across the study area, examples of which are shown in **Figure 3**, we interpret these waves as  $SS_R$  waves, where the P-to-S conversion is likely occurring at the seafloor in the absence of appreciable sediments. In the presence of appreciable sediments, the P-to-S conversion is most likely to occur along the downgoing ray path at the

base of sediments (referred to as a pSS<sub>R</sub> wave, where the path “p” is within the sediments), since a P-to-S conversion at the water-sediment interface is not likely to be efficient. Further traveltimes modelling suggest that greater sediment thickness (>50 m) will decrease the overall traveltime of the wave and not produce the observed ‘water-wave parallel’ arrivals. Hence we state that the sediment layer, within the bounds of our experiment, is thinner than 50 m, and that the observed PP and SS phases are reflections from a sub-basement interface.

We used PP and SS traveltimes picks (made within 0.05 s uncertainty) to invert for the average S-wave velocity and reflector depths. We performed a grid search to reduce the misfit between calculated and observed traveltimes of PP and SS phases. An estimate of the P-wave velocity under each a station was taken from the tomography results of Dunn et al. (2013). The error in estimating  $V_{S1}$  and  $H_1$  due to error in PP and SS traveltimes picking was under 12% (with  $\pm 0.05$ s of picking error). The outcome of this modelling for all stations is given in **Appendix D**.

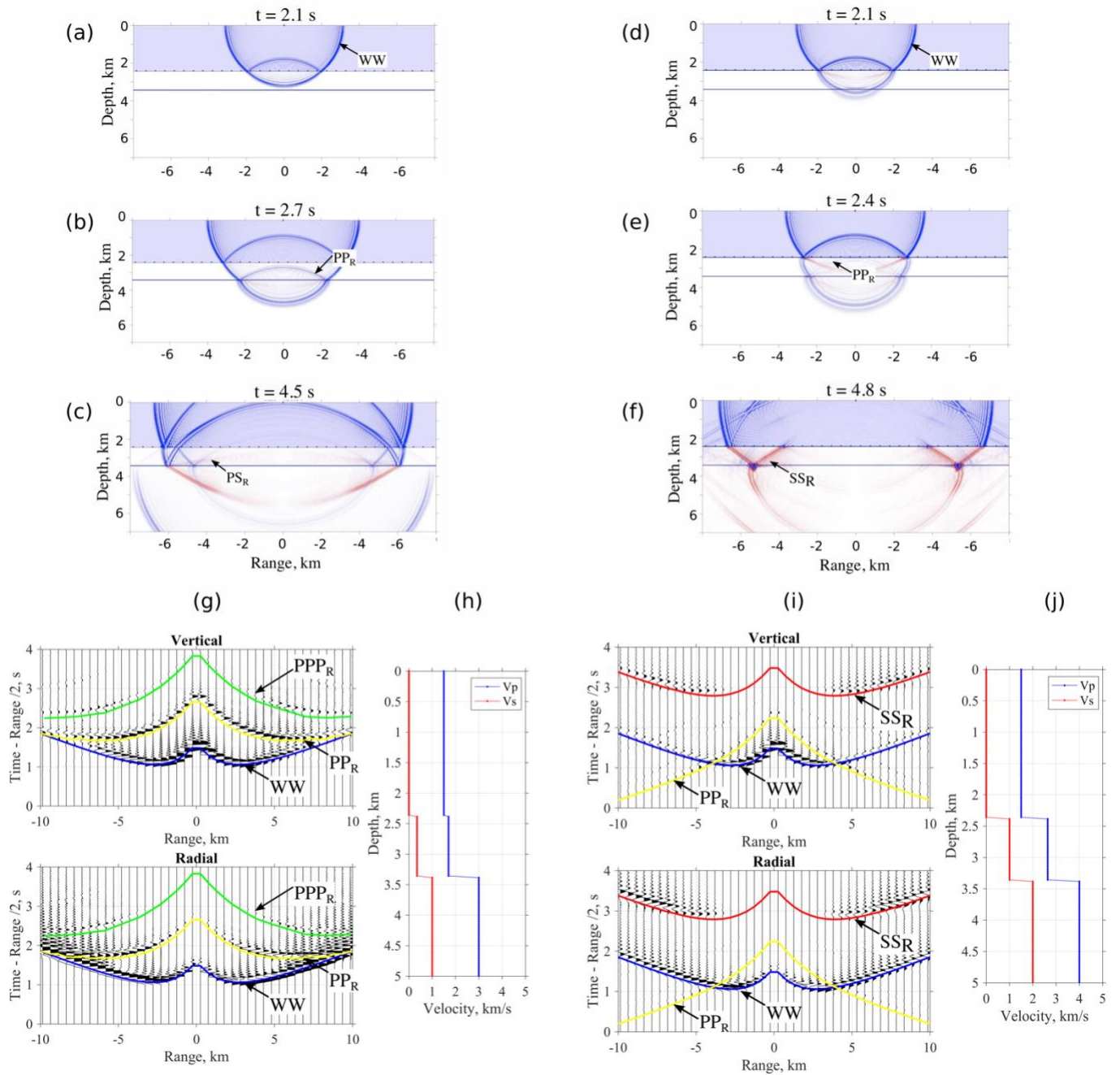


**Figure 7.** Numerically simulated elastic wavefields and seismic source gathers within 10 km range from receiver for the same 2 models in **Figure 6**. A point source at (0,0) generates waves recorded by receivers located at seafloor at 2.4 km depth with 500 m inter-spacing. Model properties are shown in **(h)** and **(j)** and the corresponding wavefields at different times are shown in **(a-c)** and **(d-f)** respectively. Labeled wavefields are direct water wave (WW), reflected P-wave ( $PP_R$ ), and reflected phase converted S-wave ( $PS_R$ ,  $SS_R$ ). **(g)** and **(i)** show common source gather for the given source-receiver geometry in the top figures for receivers for ranges up to 10 km. Also overlying the gathers

are travel time curves of WW (blue), PP<sub>R</sub> (yellow), PPP<sub>R</sub> (green), and SS<sub>R</sub> (red) phases, obtained by ray tracing.

## 5.2 Far-range Data

Preliminary traveltimes modelling of the upgoing Ps phase (in **Figure 4**), suggested that the depth of the interface where the conversion occurs could be shallow, such as the base of a sediment layer. Once we interpreted the near range data using the method described in **Section 5.1**, and calculated the near surface properties, we found that the traveltimes delay caused by the near surface layer was not able to fully explain the overall traveltimes delay observed between the P and Ps phases. Hence the conversion interface for the far range data must be deeper than the reflection interface calculated from the near-range data, such as the layer 2A/2B transition. We performed a preliminary analysis using the solutions to Zoeppritz equations on the relative amplitude of P-to-S converted wave at the base of a volcanic layer with respect to the upgoing P-wave (**Figure 8a**). Assuming fixed Layer 2B properties ( $Vp_3 = 4.5$  km/s,  $Vs_3 = 2.5$  km/s,  $\rho_3 = 2600$  kg/m<sup>3</sup>), we varied the upper crustal properties  $Vp_2$ ,  $Vs_2$  and  $\rho_2$  (refer to caption of **Figure 8**). Estimates of the incidence angle of crustal refractions at the station (from polarisation analysis) provides a rough estimate of the range of possible ray parameters for Ps phase conversion (**Figure 8b**). Within this range of interest, we find that P-to-S conversion is more efficient as the ray parameter, or incidence angle, of the upgoing wave increases, and that the converted wave's amplitude is greater for greater velocity contrasts between the lower and upper layers.

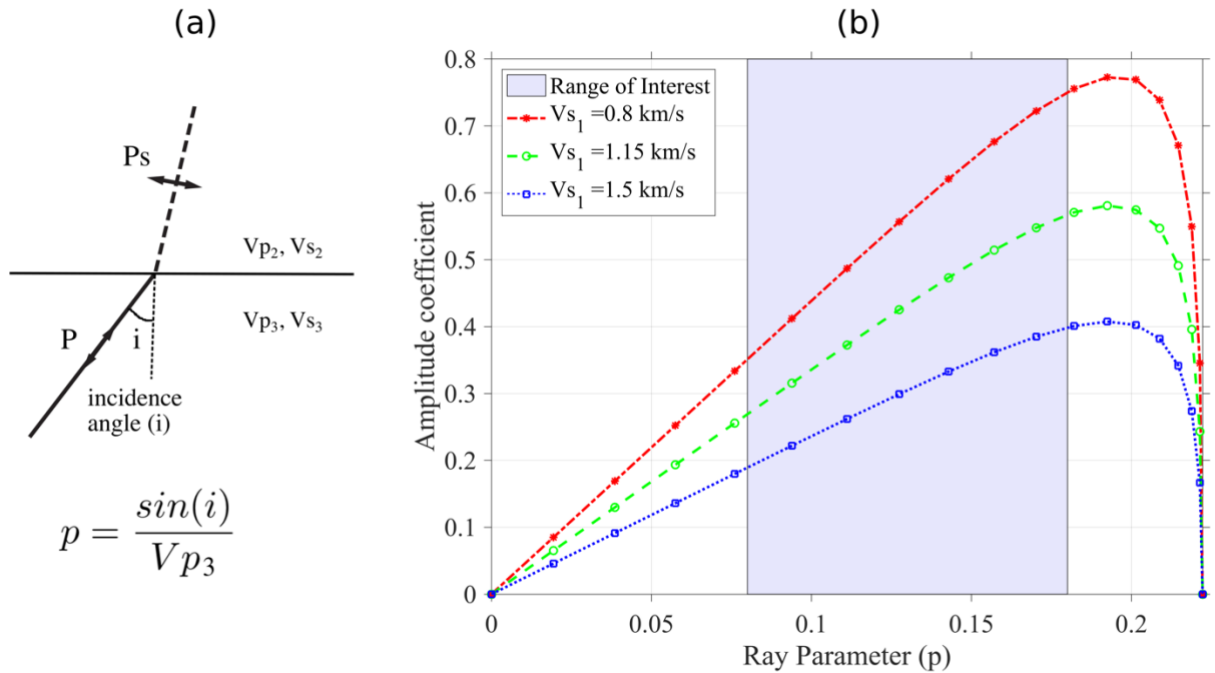


**Figure 8.** Zoeppritz solutions for an upgoing wave. **(a)** Schematic ray diagram representing P-to-S conversion of an upgoing crustal refraction at the base of layer 2A. **(b)** Relative amplitude of Ps with respect to the P phase at different ray parameters (related to incidence angle by the equation in **(a)**). Properties in the lower halfspace are fixed to  $Vp_3 = 4.5$  km/s,  $Vs_3 = 2.5$  km/s,  $\rho_3 = 2600$  kg/m<sup>3</sup>. Transmission into the upper halfspace with increasing medium impedance properties is shown: red

( $Vp_2 = 2.6$  km/s,  $Vs_2 = 0.8$  km/s,  $\rho_2 = 2230$  kg/m<sup>3</sup>), green ( $Vp_2 = 2.9$  km/s,  $Vs_2 = 1.15$  km/s,  $\rho_2 = 2330$  kg/m<sup>3</sup>) and blue ( $Vp_2 = 3.3$  km/s,  $Vs_2 = 1.5$  km/s,  $\rho_2 = 2400$  kg/m<sup>3</sup>). The range of ray parameters shown by the blue shaded region correspond to observed ray parameters of the incident P-wave at the receiver.

Since we need more information about the Ps phase and its multiples (**Figure 9a**) to get a unique estimate of layer thickness ( $H_2$ ) and  $Vp/Vs$  value in this layer, we again used solutions to Zoeppritz equations to identify the most strongly arriving waves. We modelled the amplitude ratios with respect to crustal (P-wave) refractions, as shown in **Figure 9b**. The lower medium was simulated as seismic layer 2B ( $Vp_3 = 4$  km/s,  $\rho_3 = 2600$  kg/m<sup>3</sup>,  $Vs_3 = 2.2$  km/s) while the upper medium was simulated as seismic layer 2A ( $Vp_2 = 2.5$  km/s,  $\rho_2 = 2200$  kg/m<sup>3</sup>,  $Vs_2 = 1.2$  km/s). We observe that as the ray parameter increases, the P-to-S conversion becomes more efficient, while P-reverberation (Pppp) amplitudes decrease. In terms of the traveltimes of these two phases, they interfere with each other when the  $Vp/Vs$  ratio is close to 3. They can be differentiated from each other based on their relative amplitudes on the vertical (or L) and radial (or Q) components. Amongst the shear wave multiples shown in **Figure 9a**, the Ppps phase is fastest to arrive, high in amplitude, and inverted in polarity. These observations helped identify Ps and Ppps phases in the radial component of the data.

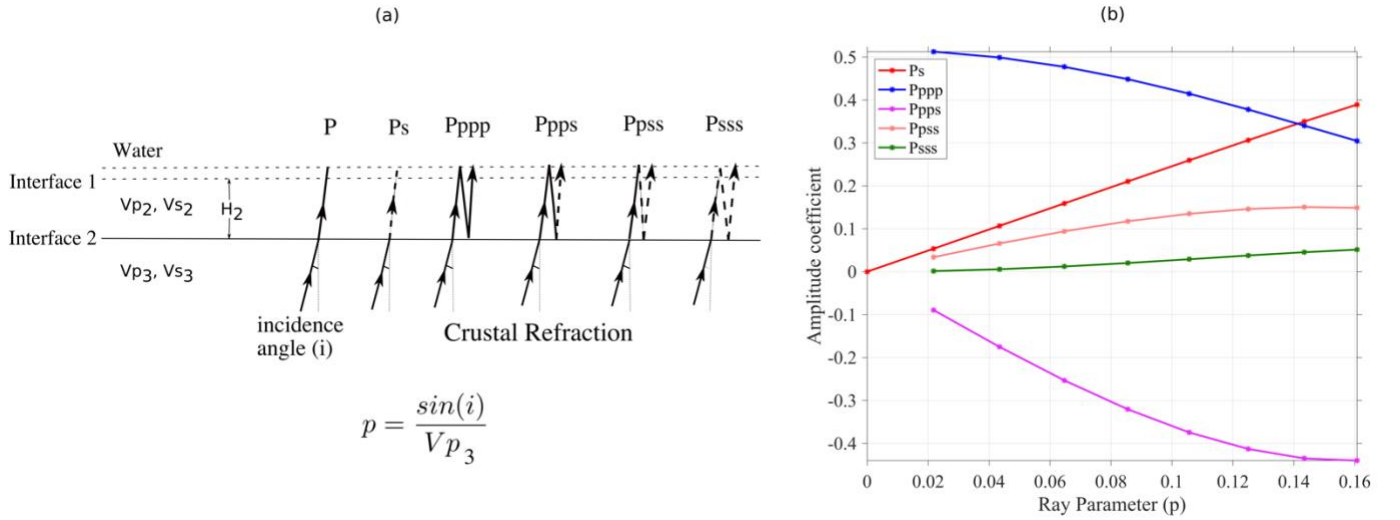


**Figure 9.** Zoeppritz solutions for an upgoing wave and its multiples. **(a)** Schematic ray diagram representing P-to-S conversions of an upgoing crustal refraction and its multiples. Solid lined ray represents P-wave and dashed lined ray represents S-wave. **(b)** Relative amplitude (as compared to the incident P wave) of converted wave primaries and multiples defined in **(a)** as a function of ray parameter. Properties in the lower halfspace and upper halfspace are fixed at  $Vp_3 = 4$  km/s,  $Vs_3 = 2.2$  km/s,  $\rho_3 = 2600$  kg/m<sup>3</sup> and  $Vp_2 = 2.5$  km/s,  $Vs_2 = 1.2$  km/s,  $\rho_2 = 2200$  kg/m<sup>3</sup> respectively.

Using the simple travel time formulas given by equations 1-2, we inverted for the layer thickness ( $H_2$ ) and interval velocity ( $V_{S2}$ ) in the upper layer, which produced the phases Ps and Ppps.  $\Delta t_{Ps}$  and  $\Delta t_{Ppps}$  are defined as their delay time with respect to crustal refracted P-wave in observed data.. The near surface properties ( $H_1$ ,  $V_{p1}$ ,  $V_{S1}$ ) were calculated as described in section 5.1. P-wave velocity in second layer ( $V_{p2}$ ) was approximated from tomography results given by Dunn et al. (2013). Due to the intermittent nature of Ps and Ppps phases, we found that they were recorded with acceptable signal-to-noise ratios at only 36 receivers spread across the study area (refer to **Section 6** for complete details)

$$\Delta t_{Ps} = H_1 \left( \frac{1}{V_{S1}} - \frac{1}{V_{p1}} \right) + H_2 \left( \frac{1}{V_{S2}} - \frac{1}{V_{p2}} \right) \quad (1)$$

$$\Delta t_{Ppps} = H_1 \left( \frac{1}{V_{S1}} + \frac{1}{V_{p1}} \right) + H_2 \left( \frac{1}{V_{S2}} + \frac{1}{V_{p2}} \right) \quad (2)$$

Uncertainty in the estimates of  $V_p/V_s$  value and layer thickness ( $H$ ) using the method described above is found to be less dependent on  $V_p$  uncertainty. For example, using a  $V_p$  of 3 km/s and a  $V_p/V_s$  ratio of 2 for a 800 m layer, the uncertainty in  $H_2$  is given by

$$\Delta H_2 = \left( \frac{\partial H}{\partial V_{p2}} \right) \Delta V_{p2} = 0.27 \Delta V_{p2} \quad (3)$$

which means the uncertainty in  $H_2$  is less than 50 m for a 0.15 km/s uncertainty in  $V_{p2}$ . The error contribution from a picking error of 0.05 s was found to be within 15% for  $H_2$  and less than 10% for  $V_p/V_s$  values.

## 6. Results

SS travel times from near offset data, which indicate variations in uppermost crustal and/or sediment layer properties ( $H_1$ ,  $V_{p1}$ ,  $V_{S1}$ ), were compiled for all available stations and are shown in **Figure 10**. Theoretically, SS-waves are not generated at zero range, hence for this figure the traveltimes along a hypothetical vertical ray path were computed from the layer thickness and velocity estimated from the wide-angle (2-10 km) data for each station. The traveltme magnitude represents the combined effect of near surface S-wave velocities and the depth of the reflector, with larger SS times (larger circles in **Figure 10**) corresponding with either lower  $V_{S1}$  values and/or a greater values of  $H_1$ . In general, smaller times are observed near the ridge, and larger times are observed away from the ridge, with some particularly large values for stations located on the east side (arc side) of the ridge axis. Also shown in **Figure 10** is a sonar image of the seafloor for the study area (Dunn et al., 2015). Smaller SS times are observed in regions with higher sonar backscatter (usually younger, un-sedimented seafloor), and larger SS times are observed in areas of very low backscatter (e.g., heavily sedimented seafloor). There is a greater range of both SS times and backscatter values on the east side, where backscatter and seafloor morphology indicate larger variations in sediment cover due to sediment ponds, topographic effects, and late stage volcanism. The largest travel times correlate with deep basins that appear to be filled with sediments.

Using the method described in **Section 5.1**, the depth to the reflector ( $H_I$ ) beneath the receiver and average S-wave velocity ( $V_{SI}$ ) were calculated within 15% uncertainty. A complete list of estimated  $H_I$  and  $V_{SI}$  values is given in **Appendix D**. **Figure 11** shows a plot of estimated values of  $H_I$  as function of distance to the ridge axis; the values are colored based on the respective station's location within the crustal domains. In general, larger  $H_I$  values are found farther from the ridge, with a greater range of values on the east side. Furthermore, the average value of  $H_I$  is greater on the eastern side of the ridge axis (~100 m) as compared to the west (~60 m). The smallest and non-zero values of  $H_I$  are found within 4 km of the ridge axis ~50 m deep. Some stations do not have an estimated  $H_I$  value due to no discernible PP wave and do not show up in **Figure 11**. The average S-wave velocity is relatively lower on the east side (~500 m/s) than the west side (~570 m/s); both being higher than values observed in pelagic and hemipelagic marine sediments (200–300 m/s; Hamilton, 1979), and lower than values observed in consolidated volcanoclastic sediment (0.8–1 km/s; Kenter and Ivanov, 1995) or layer 2A (1.5-2 km/s; Spudich & Orcutt, 1980).

In regions devoid of sediments (i.e. along the ridge axis), the near surface layer (of thickness  $H_I$ ) is a low-velocity surface layer within the igneous crustal layer 2A, which we refer to as 'Layer 2Aa'. In the presence of sediments, the reflections are possibly still coming from the base of Layer 2Aa. The layer 2Aa is too shallow to be consistent with a layer 2A/2B boundary (Jacobs et al., 2007). P-waves reflecting from such a thin layer would arrive within <50 ms of the seafloor reflection in multi-channel seismic data, making the reflector difficult to observe in reflection images. S waves, on the other hand, will arrive later at ~200 ms behind the water wave, providing enough phase separation for the reflected arrivals to be obvious in most cases. At 20 Hz, S waves also have much smaller wavelengths (22 m) than corresponding P waves (~100 m), enhancing their ability to be reflected from the bottom of a thin (<50 m) surface layer.

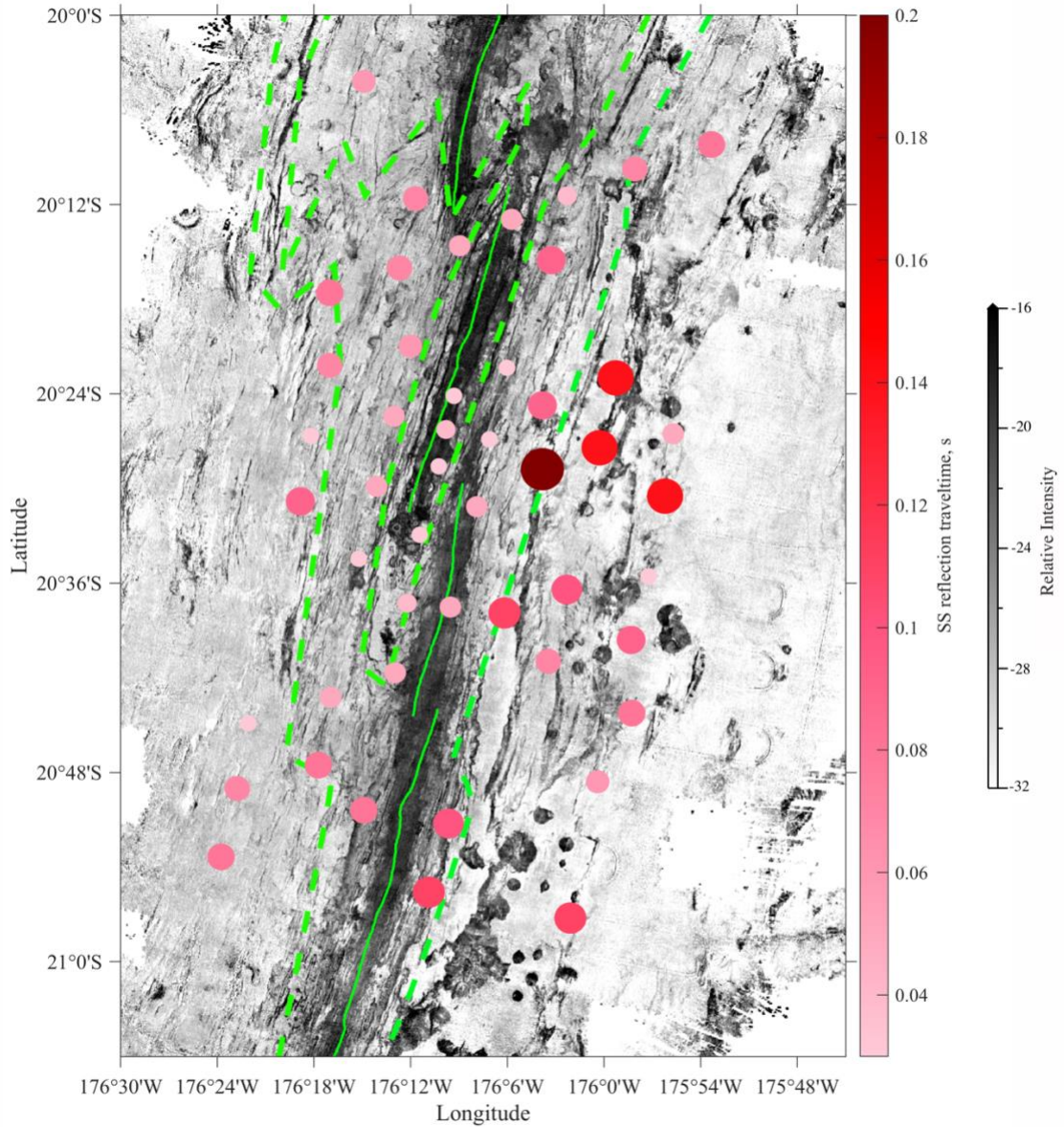


**Figure 10.** Sonar image of the study area and observed SS traveltimes for each station. The size of each circle is proportional to the estimated vertical, two-way-traveltime for the layer thickness and velocity estimated from the wide-angle (2-10 km) data. The axis of the spreading center is shown by a solid green line, and the different crustal domains are separated by dashed green lines. In the sonar image (from Dunn et al., 2015), darker colors indicate higher sonar return (e.g., young un-sedimented seafloor) and lighter colors indicate lower sonar return (e.g., heavily sedimented seafloor).

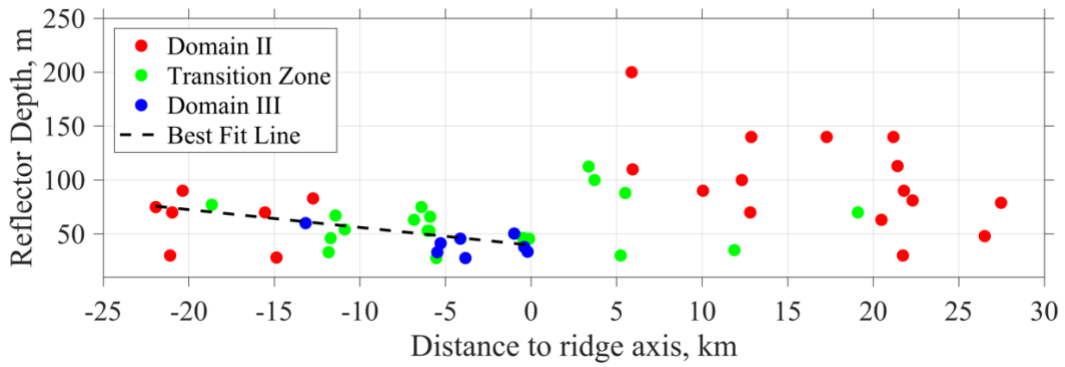


**Figure 11.** Reflector depths (in m) beneath a station versus a station’s distance to the ridge axis for the different crustal domains: Domain II (red), Transition Zone (green) and Domain III (blue). Also shown is the best fit line, made using a robust regression fitting method (Holland and Welsch, 1977), through the data on the west side of the ridge axis.

When interpreting the second kind of shear wave arrivals, i.e. the far-range crustal refracted and converted arrivals (**Figure 4**), the traveltimes between P and Ps phases were 0.13-0.58 s greater than delays calculated from the near-surface layer properties ( $H_1$ ,  $V_{s1}$ ,  $V_{p1}$ ). Therefore, P-to-S conversion depths of the Ps arrivals must be deeper than  $H_1$ . Using the method described in **Section 5.2**, we found that Ps and Ppps arrivals were explained by a conversion (Ps) and subsequent multiple generation (Ppps) at depths ( $H_2$ ) consistent with a layer 2A to 2B transition. Estimated depths for the 2A/2B transition (~500-700 m) are consistent with those determined by Jacobs et al. (2007), where available.

**Figure 12a** shows estimated layer 2A thickness values overlain on a map view tomographic slice of upper crustal P-wave velocities (Dunn et al., 2013). In general, layer 2A is observed to be relatively thicker in regions of low P-wave velocities and thinner in regions of high P-wave velocities, roughly corresponding to the crustal domain designations. **Figure 12b** shows estimated  $V_p/V_s$  values in layer 2A overlain on a map view tomographic slice of upper crustal P-wave velocities.  $V_p/V_s$  values greater than 2.6 (red colors) are observed to spatially correlate with regions of low P-wave velocities.  $V_p/V_s$  values less than 2.6 (blue colors) are observed to spatially correlate with regions of high P-wave velocity. The correlation between layer 2A thicknesses,  $V_p/V_s$  values, and crustal domains is further demonstrated in **Figure 13**, where thinner layers (~500 m, on average) with lower  $V_p/V_s$  (~2.3, on average) are found in Domain III and thicker layer values (~650 m, on average) and higher  $V_p/V_s$  (~3.0, on average) are found in Domain II. Complete list of estimated  $H$  and  $V_s$  values of layer 2A is provided in **Appendix E**.

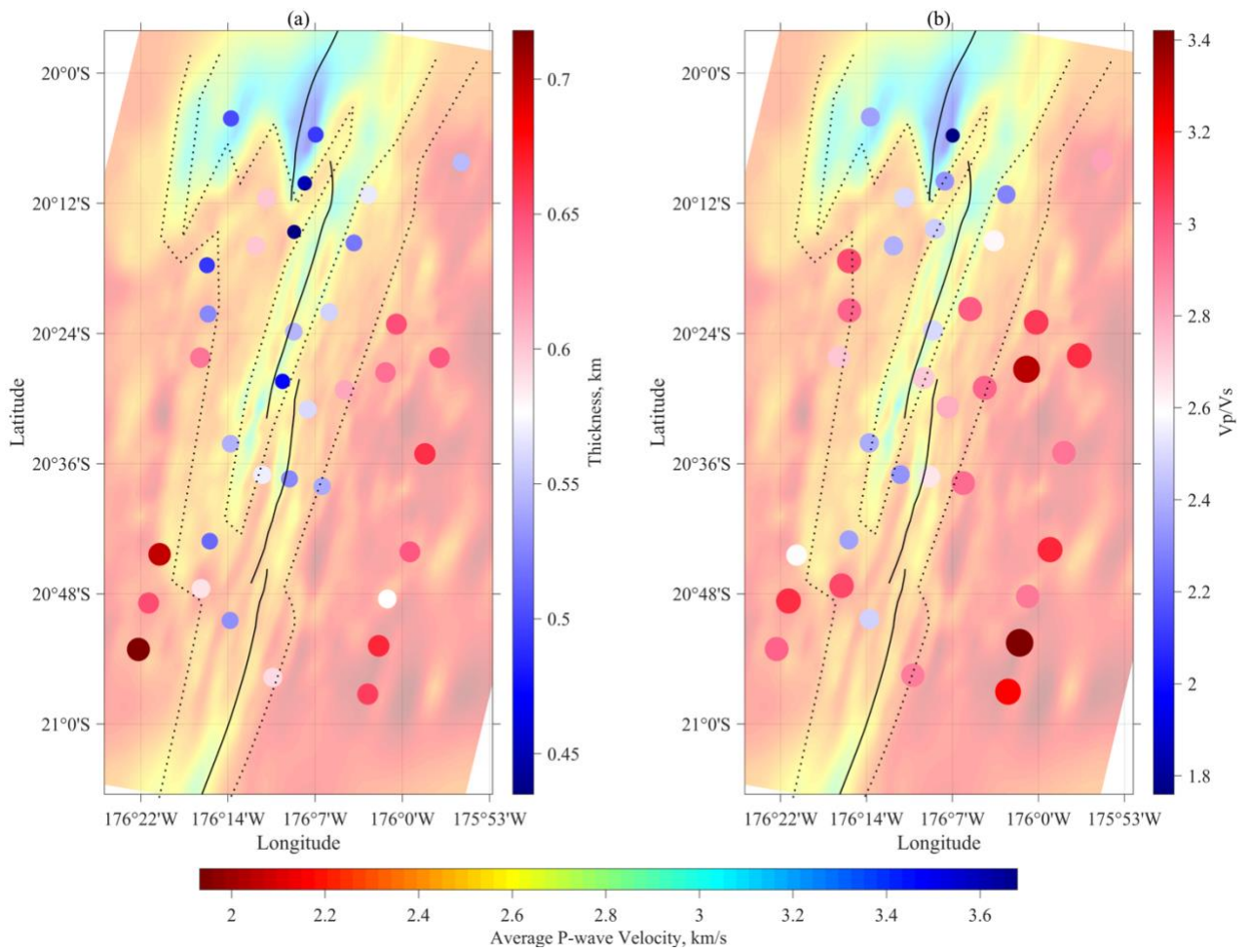


**Figure 12.** Layer 2A estimated thicknesses **(a)** and  $V_p/V_s$  values **(b)** overlain on a map view tomographic slice of upper crustal P-wave velocities (from Dunn et al., 2013). Location of each circle corresponds to the location of the receiver. In the tomographic image, velocity values are averaged in the depth range of 250 m to 500 m of crust. The axis of the spreading center is shown by the thin black line. Only the values for 35 stations with recorded good signal-to-noise ratios for Ps and Ppps phases are used.

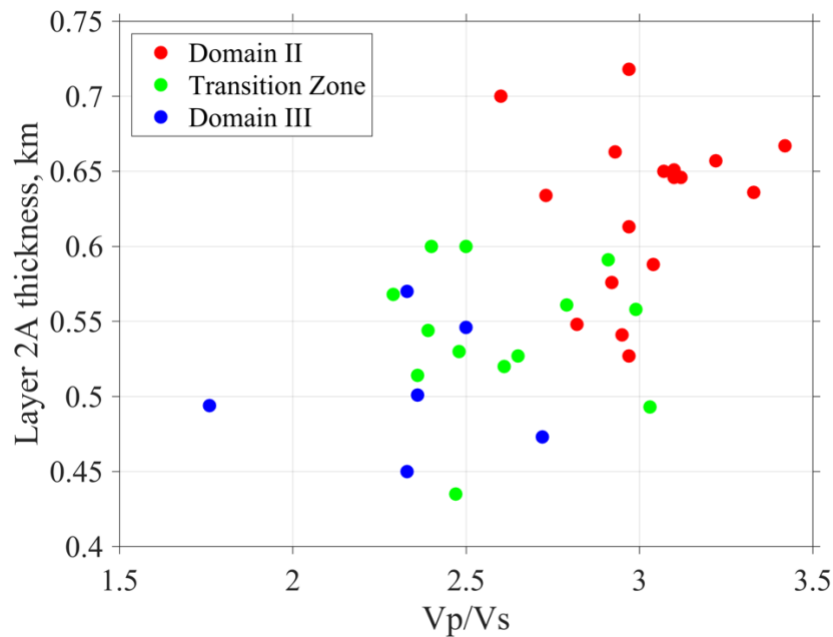


**Figure 13.** Scatter plot of layer 2A thickness (in km) versus  $Vp/Vs$  across the study area, highlighting differences between the crustal domains.

## 7. Discussion

### 7.1 Near Surface Layer

Few estimates of sediment thickness in the region are available. ROV images detect little to no sediment near the ridge axis (Ferrini et al., 2008). Backscatter images also indicate a sediment free spreading center, with increasing sediment coverage at greater crustal ages and greater coverage on the arc-side of the ridge (Martinez et al., 2006). In the off axis regions, sub-bottom profile data from recent cruises to the area do not penetrate to basement in sedimented regions and thus can only provide crude estimates of minimum sediment thickness. Drill log data from a site located 50 km west of the ridge axis, in Domain III, found a ~20 m sequence of clayey nannofossil oozes with interbedded turbiditic volcanic sands and silts, pyroclastic ashes, and thick-bedded mafic hyaloclastites overlying a MORB-like igneous basement (Hawkins 1994), suggesting sedimentation on the western side of the ridge is not heavily influenced by arc volcanic debris. Examining the backscatter and topography together, and estimating the degree of sedimentation from the degree of in-filling of local topography, suggests that the western side of the ridge within the seismic array is only lightly draped by sediment with increasing age, whereas the eastern side is more heavily draped with some broad valleys with significant accumulation.

Across the seismic experiment, for areas either with or without appreciable sediment coverage, our analysis points to the existence of a shallow low-velocity layer at the top of the crust. The low efficiency of P-to-S conversions at the top of sediment indicate a deeper source for the conversion point and an even deeper intra-crustal point for the observed S-S reflection. Therefore we suggest that the conversion point for P-to-S waves is at the top of the igneous crust, even in sedimented regions, and the S-S reflection horizon is within the igneous crust. Travel times of reflected

waves would, nevertheless, be influenced by sediment thickness. On the western side of the ridge axis, where sediment cover is obvious in backscatter images, travel times increase with crustal age, as expected for slow accumulation of sediment. On the eastern side of the ridge, travel times are larger and more variable, as expected for the enhanced accumulation rate of volcanoclastic sediments from the active arc, especially if they preferentially fill local basins. Based on our seismic observations and drawing inferences from all available information, we conclude that the sediment cover on the western side of ridge axis is generally less than 20 m thick, and gradually reduces to 0 m towards ridge axis as the seafloor becomes younger. On the eastern side of ridge axis, sediment cover is variable, ranging between 0 – 50 m, with the exception of some deeper sediment ponds, where it could be substantially thicker. A relatively thicker sediment cover on the east is expected due to the proximity to the Tofua Arc.

**Layer 2Aa:** The seafloor along the ridge axis is devoid of sediments, as indicated by the backscatter image and ROV dives (Martinez et al., 2006; Ferrini et al., 2008), nevertheless a subsurface shallow reflector (~80 m deep) is consistently found beneath all the stations sitting on the ridge axis. In addition, this reflector is also present in the off-axis regions, as indicated by the inherent inefficiency of the water-sediment interface to produce a significant down going S wave. The SS reflector is much shallower than estimated depths to the base of layer 2A (500–700 m; Jacobs et al., 2007). A study using a full waveform inversion method for data collected along the Mid-Atlantic Ridge has also identified a thin (50-150 m thick) low-velocity crustal layer at the top of seismic layer 2A (Arnulf et al., 2012) that they refer to as seismic layer 2Aa, the name we adopt here. This layer could represent a more porous extrusive lava layer on top of a less porous lava layer below, where the difference arises perhaps due to a compaction process. For example, thin cracks created by thermal stresses during lava cooling are easier to close with increasing pressure than more spherical void space (Wilkins et al., 1991), perhaps allowing for a rapid change in seismic properties with increasing confining pressure at shallow depths, followed by a more gradual change at greater depth.

## 7.2 Layer 2A

The thickness of layer 2A is often considered to be a proxy for the thickness of the volcanic, extrusive layer of lavas in the upper oceanic crust. In Domain II, where the crust is overall thicker (~8–9.5 km), layer 2A is also thicker (~650 m average), whereas the thinner crust in Domain III (~5.5–6 km) also has a thinner layer 2A (~500 m average). The rate of melt supply to the spreading center likely influences the volcanic layer thickness, such that a higher melt supply leads to a thicker volcanic layer. The increase in layer 2A thickness with crustal thickness is not proportional, and the factors influencing the ratio of extrusive crustal growth to intrusive crustal growth at the ridge axis are not entirely clear.

The pattern of layer 2A thickness strongly correlates with the pattern of estimated S-wave velocities, with lower  $V_s$  values (~0.9 km/s) in Domain II as compared to Domain III (~1.2 km/s). Seismic velocities in layer 2A are thought to be largely controlled by porosity and the shapes of the voids and cracks (Shearer, 1988), with lower velocities in more porous rocks. This suggests that a more porous and thicker volcanic layer of lavas cap the thicker crust in Domain II and a thinner less porous layer of lavas cap the crust in Domain III. Estimated  $V_p/V_s$  values in the volcanic layer are higher in Domain II (~3.0) as compared to Domain III (~2.3). Poisson's ratio ( $\nu$ ), related to  $V_p/V_s$  ratio by

equation (4) for isotropic medium, is used as an indicator of rock lithology and composition (e.g. Christensen, 1996; Collier and Singh, 1998; Kim et al., 2018).

$$v = \frac{1}{2} \left( \frac{k^2 - 2}{k^2 - 1} \right) \quad ; \quad k = \frac{Vp}{Vs} \quad (4)$$

From the estimated values of  $Vp/Vs$ , we find that Poisson's ratio is  $\sim 0.44$  and  $\sim 0.38$  in the upper layer of extrusive basalts of Domain II and Domain III respectively. Although a direct relationship of rock porosity with average Poisson's ratio is highly non-unique, comparisons from different settings can help us understand their relative influence. For example, a seismic study by Collier and Singh (1988) on the ridge axis of East Pacific Rise found average Poisson's ratios of 0.34 in layer 2A. While this value is closer to our estimates for Domain III layer 2A, Poisson's ratios in Domain II are much higher. A likely cause for the anomalously high Poisson's ratio in Domain II layer 2A is its high porosity (e.g. Peacock et al., 2011). This is corroborated by the highly vesicular nature of lava samples dredged from Domain II crust (Pearce et al., 1994).

In addition, the observed variation in  $Vp/Vs$  values may also be influenced by variations in major element composition. Jacobs et al. (2007) estimated that approximately half of the observed 0.6 km/s decrease in P-wave velocity in layer 2B, along the ridge axis could be attributed to compositional variations, while attributing the other half to a change in intrinsic porosity. Major element compositions for lavas sampled along the ridge axis change from basaltic to basaltic-andesite as the distance to the arc decreases. Our  $Vp/Vs$  values change approximately with this trend, although most of the major element trend extends beyond the study area. However, our maps of  $Vp/Vs$  variations that extend off axis could then show significant major element chemistry changes from Domain II to III. That is to say, Domain II may have a basaltic-andesite cap of lavas as compared to a basaltic cap of lavas in Domain III. Whether due mostly to porosity changes or to porosity and major element changes is not clear in the absence of off-axis lava samples of crust formed at the spreading center, nevertheless the patterns in the seismic (and other geophysical data) are clear and suggest significantly different crustal formation processes in the near arc regions versus distal regions.

### 7.3 Subduction Influence on Upper Crustal Structure

In a mid-oceanic ridge system, decompression melting is the main source of magma production, wherein convection driven mantle material experience a decrease in pressure which leads to partial melting. Hence seafloor spreading rate, one of the factors that drives convection, plays an important role in magma production, and subsequent crustal formation. On the other hand, in a back arc setting, slab-derived volatiles (mainly water) reduces mantle melting temperature leading to enhanced melt production. Along the ELSC, the added effect of hydrous flux melting may produce up to  $\sim 30\%$  more crust (Arai and Dunn, 2014), and differences in magma supply and subsequent crustal structure is related to distance from the arc volcanic front, rather than spreading rate (Martinez and Taylor, 2006). Our estimates of layer 2A thickness and shear wave velocities in Domain II further strengthen this hypothesis. Since Domain II crust was formed when the ridge axis was closer to the volcanic arc, the volcanic layer shows a strong influence from slab-derived volatiles in the form of higher porosity (lower velocities and higher  $Vp/Vs$ ). The presence of water during melting is expected to increase melt production (e.g., Davies and Bickle, 1991; Stolper and Newman,

1994). This is corroborated by the thicker volcanic layer in Domain II as compared to Domain III. In Domain III, faster velocities, lower  $Vp/Vs$ , and a thinner volcanic layer indicate a waning influence of slab derived volatiles; and the interpretation is that the ridge has moved farther away from the subducting slab the influence of slab-derived volatiles on crustal structure.

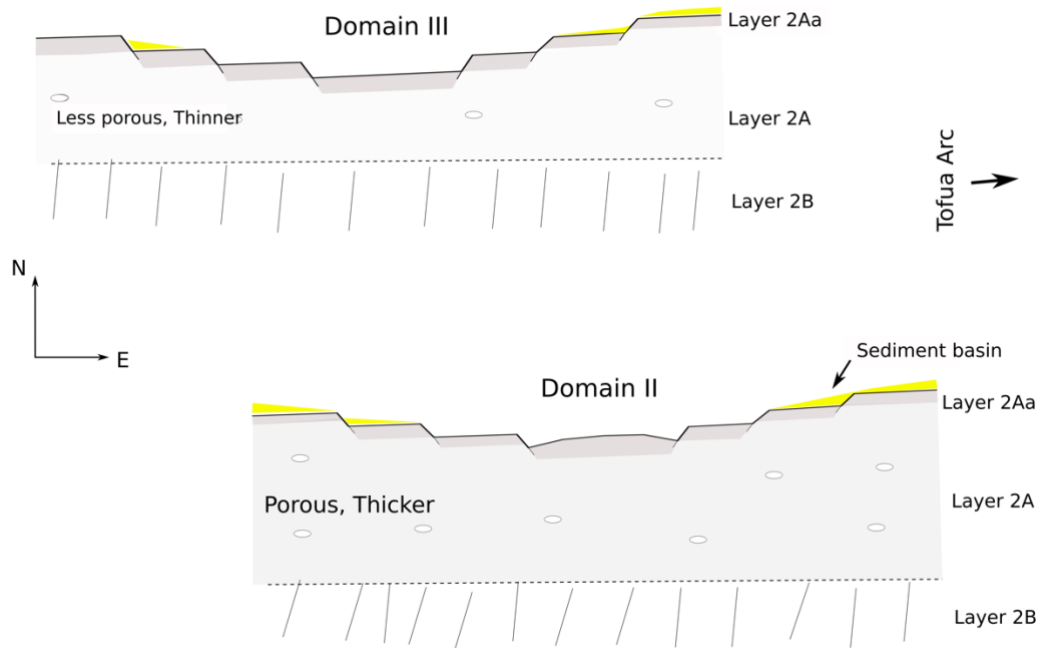


**Figure 14.** Cartoon interpretation of sediment layer and upper crustal structure as a function of arc proximity. The shallowest seismic layer 2Aa is consistently present across the study area. At the southern ridge segment (foreground), the sediment cover in the off axis regions is greater in the east as compared to the west. The more thickly sedimented region on the east is closer to the volcanic Tofua arc. A thicker and more porous pillow lava layer (seismic layer 2A) underlies layer 2Aa as compared to the northern ridge segment (background), where a thinner and less porous pillow lava layer (seismic layer 2A) is present. This region is away from the volcanic Tofua arc.

## 8. Conclusions

S-wave data, in the form of P-to-S conversions, collected as part of L-SCAN active-source seismic experiment reveal large domain-specific upper crustal variations. This study compliments previous studies on bathymetry, gravity, sonar backscatter, seismic and chemistry, and presents new evidence on upper crustal layer 2A thickness and  $Vp/Vs$  values across the previously identified crustal domains. Both layer 2A thickness and  $Vp/Vs$  values tend to correlate with these domains. The results show strong evidence for the influence of slab-derived water on crustal formation at the Eastern Lau Spreading Center when it is located closer to the arc, as compared to the waning influence on crust formed at locations away from the arc.

## References

- Aki, K., and P.G. Richards. 1980. *Quantitative Seismology*. W. H. Freeman & Co.
- Anderson, P. N., F. K. Duennebie, and R. K. Cessaro. 1987. "Ocean Borehole Horizontal Seismic Sensor Orientation Determined from Explosive Charges." *Journal of Geophysical Research* 92 (B5): 3573.  
<https://doi.org/10.1029/JB092iB05p03573>.
- Arai, Ryuta, and Robert A. Dunn. 2014. "Seismological Study of Lau Back Arc Crust: Mantle Water, Magmatic Differentiation, and a Compositionally Zoned Basin." *Earth and Planetary Science Letters* 390 (March): 304–17. <https://doi.org/10.1016/j.epsl.2014.01.014>.
- Arnulf, A. F., A. J. Harding, S. C. Singh, G. M. Kent, and W. Crawford. 2012. "Fine-Scale Velocity Structure of Upper Oceanic Crust from Full Waveform Inversion of Downward Continued Seismic Reflection Data at the Lucky Strike Volcano, Mid-Atlantic Ridge: LAYER 2A STRUCTURE, MID-ATLANTIC RIDGE." *Geophysical Research Letters* 39 (8): n/a-n/a. <https://doi.org/10.1029/2012GL051064>.
- Austin, Regan. 2012. "EARLY SEAFLOOR SPREADING AND VARIATIONS IN CRUSTAL ACCRETION IN THE LAU BASIN." [http://www.soest.hawaii.edu/GG/academics/theses/MS\\_2012\\_Austin.pdf](http://www.soest.hawaii.edu/GG/academics/theses/MS_2012_Austin.pdf).
- Becker, Nathan C., Patricia Fryer, and Gregory F. Moore. 2010. "Malaguana-Gadao Ridge: Identification and Implications of a Magma Chamber Reflector in the Southern Mariana Trough." *Geochemistry, Geophysics, Geosystems* 11 (4). <https://doi.org/10.1029/2009GC002719>.
- Berge, Patricia A., Gerard J. Fryer, and Roy H. Wilkens. 1992. "Velocity-Porosity Relationships in the Upper Oceanic Crust: Theoretical Considerations." *Journal of Geophysical Research* 97 (B11): 15239.  
<https://doi.org/10.1029/92JB01464>.
- Bratt, Steven R., and Sean C Solomon. 1984. "Compressional and Shear Wave Structure of the East Pacific Rise at 1120N Constraints from Three component Ocean Bottom Seismometer Data," 16.
- Christensen, Nikolas I. 1978. "Ophiolites, Seismic Velocities and Oceanic Crustal Structure." *Tectonophysics* 47 (1–2): 131–57. [https://doi.org/10.1016/0040-1951\(78\)90155-5](https://doi.org/10.1016/0040-1951(78)90155-5).
- Christensen, Nikolas I. 1996. "Poisson's Ratio and Crustal Seismology." *Journal of Geophysical Research: Solid Earth* 101 (B2): 3139–56. <https://doi.org/10.1029/95JB03446>.
- Christeson, G. L., G. M. Kent, G. M. Purdy, and R. S. Detrick. 1996. "Extrusive Thickness Variability at the East Pacific Rise, 9°-10°N: Constraints from Seismic Techniques." *Journal of Geophysical Research: Solid Earth* 101 (B2): 2859–73. <https://doi.org/10.1029/95JB03212>.
- Christeson, G. L., G. M. Purdy, and G. J. Fryer. 1994. "Seismic Constraints on Shallow Crustal Emplacement Processes at the Fast Spreading East Pacific Rise." *Journal of Geophysical Research: Solid Earth* 99 (B9): 17957–73. <https://doi.org/10.1029/94JB01252>.
- Christeson, G. L., P. R. Shaw, and J. D. Garmany. 1997. "Shear and Compressional Wave Structure of the East Pacific Rise, 9°-10°N." *Journal of Geophysical Research: Solid Earth* 102 (B4): 7821–35.  
<https://doi.org/10.1029/96JB03901>.

- Christeson, G. L., W. S. D. Wilcock, and G. M. Purdy. 1994. "The Shallow Attenuation Structure of the Fast-Spreading East Pacific Rise near 9°30'N." *Geophysical Research Letters* 21 (5): 321–24.  
<https://doi.org/10.1029/94GL00189>.
- Christeson, Gail L., Jeffrey A. Karson, and Kirk D. McIntosh. 2010. "Mapping of Seismic Layer 2A/2B Boundary above the Sheeted Dike Unit at Intermediate Spreading Crust Exposed near the Blanco Transform: MAPPING SEISMIC LAYER 2A/2B BOUNDARY." *Geochemistry, Geophysics, Geosystems* 11 (3): n/a-n/a.  
<https://doi.org/10.1029/2009GC002864>.
- Christeson, Gail L., Kirk D. McIntosh, and Jeffrey A. Karson. 2007. "Inconsistent Correlation of Seismic Layer 2a and Lava Layer Thickness in Oceanic Crust." *Nature* 445 (7126): 418–21. <https://doi.org/10.1038/nature05517>.
- Coleman, R. G. 2012. *Ophiolites: Ancient Oceanic Lithosphere?* Springer Science & Business Media.
- Coleman, R.G. 1977. *Ophiolites, Ancient Oceanic Lithosphere?* Springer.
- Collier, J. S., and S. C. Singh. 1998. "Poisson's Ratio Structure of Young Oceanic Crust." *Journal of Geophysical Research: Solid Earth* 103 (B9): 20981–96. <https://doi.org/10.1029/98JB01980>.
- Davies, J. Huw, and M. J. Bickle. 1991. "A Physical Model for the Volume and Composition of Melt Produced by Hydrous Fluxing above Subduction Zones." *Philosophical Transactions: Physical Sciences and Engineering* 335 (1638): 355–64.
- Detrick, R., J. Collins, R. Stephen, and S. Swift. 1994. "In Situ Evidence for the Nature of the Seismic Layer 2/3 Boundary in Oceanic Crust." *Nature* 370 (6487): 288–90. <https://doi.org/10.1038/370288a0>.
- Detrick, Robert S., Douglas R. Toomey, and John A. Collins. 1998. "Three-Dimensional Upper Crustal Heterogeneity and Anisotropy around Hole 504B from Seismic Tomography." *Journal of Geophysical Research: Solid Earth* 103 (B12): 30485–504. <https://doi.org/10.1029/98JB02409>.
- Dilek, Y., and H. Furnes. 2011. "Ophiolite Genesis and Global Tectonics: Geochemical and Tectonic Fingerprinting of Ancient Oceanic Lithosphere." *Geological Society of America Bulletin* 123 (3–4): 387–411.  
<https://doi.org/10.1130/B30446.1>.
- Dunn, Robert A. 2015. "Tracking Stress and Hydrothermal Activity along the Eastern Lau Spreading Center Using Seismic Anisotropy." *Earth and Planetary Science Letters* 410 (January): 105–16.  
<https://doi.org/10.1016/j.epsl.2014.11.027>.
- Dunn, Robert A., and Fernando Martinez. 2011. "Contrasting Crustal Production and Rapid Mantle Transitions beneath Back-Arc Ridges." *Nature* 469 (7329): 198–202. <https://doi.org/10.1038/nature09690>.
- Dunn, Robert A., Fernando Martinez, and James A. Conder. 2013. "Crustal Construction and Magma Chamber Properties along the Eastern Lau Spreading Center." *Earth and Planetary Science Letters* 371–372 (June): 112–24. <https://doi.org/10.1016/j.epsl.2013.04.008>.
- Eason, Deborah E., and Robert A. Dunn. 2015. "Petrogenesis and Structure of Oceanic Crust in the Lau Back-Arc Basin." *Earth and Planetary Science Letters* 429 (November): 128–38.  
<https://doi.org/10.1016/j.epsl.2015.07.065>.

- Eccles, Jennifer D., Robert S. White, and Philip A. F. Christie. 2009. "Identification and Inversion of Converted Shear Waves: Case Studies from the European North Atlantic Continental Margins." *Geophysical Journal International* 179 (1): 381–400. <https://doi.org/10.1111/j.1365-246X.2009.04290.x>.
- Escrig, S., A. Bézoz, S. L. Goldstein, C. H. Langmuir, and P. J. Michael. 2009. "Mantle Source Variations beneath the Eastern Lau Spreading Center and the Nature of Subduction Components in the Lau Basin-Tonga Arc System: ISOTOPE GEOCHEMISTRY OF LAU BASIN LAVAS." *Geochemistry, Geophysics, Geosystems* 10 (4): n/a-n/a. <https://doi.org/10.1029/2008GC002281>.
- Ferrini, Vicki Lynn, Margaret K. Tivey, Suzanne M. Carbotte, Fernando Martinez, and Chris Roman. 2008. "Variable Morphologic Expression of Volcanic, Tectonic, and Hydrothermal Processes at Six Hydrothermal Vent Fields in the Lau Back-Arc Basin." *Geochemistry, Geophysics, Geosystems* 9 (7). <https://doi.org/10.1029/2008GC002047>.
- Gaetani, G. A., and T. L. Grove. 1994. "Melting in the Sub-Arc Mantle: The Effects of H<sub>2</sub>O on Primary Magmas and the Spinel-to-Garnet Transition." *Mineralogical Magazine* 58A (1): 301–2. <https://doi.org/10.1180/minmag.1994.58A.1.158>.
- Guevara, Saul E, and Robert R Stewart. 1998. "Multicomponent Seismic Polarization Analysis" 10: 19.
- Hamilton, Edwin L. 1979. " $V_p/V_s$  and Poisson's Ratios in Marine Sediments and Rocks." *The Journal of the Acoustical Society of America* 66 (4): 1093–1101. <https://doi.org/10.1121/1.383344>.
- Harding, Alistair J., Graham M. Kent, and John A. Orcutt. 1993. "A Multichannel Seismic Investigation of Upper Crustal Structure at 9°N on the East Pacific Rise: Implications for Crustal Accretion." *Journal of Geophysical Research: Solid Earth* 98 (B8): 13925–44. <https://doi.org/10.1029/93JB00886>.
- Hawkins, J., L. Parson, J. Allan, and et al., eds. 1994. *Proceedings of the Ocean Drilling Program, 135 Scientific Results*. Vol. 135. Proceedings of the Ocean Drilling Program. Ocean Drilling Program. <https://doi.org/10.2973/odp.proc.sr.135.1994>.
- Hawkins, James W. 1995. "Evolution of the Lau Basin: Insights from ODP Leg 135." In *Geophysical Monograph Series*, edited by Brian Taylor and James Natland, 88:125–73. Washington, D. C.: American Geophysical Union. <https://doi.org/10.1029/GM088p0125>.
- Hirth, Greg, and David L. Kohlstedt. 1996. "Water in the Oceanic Upper Mantle: Implications for Rheology, Melt Extraction and the Evolution of the Lithosphere." *Earth and Planetary Science Letters* 144 (1–2): 93–108. [https://doi.org/10.1016/0012-821X\(96\)00154-9](https://doi.org/10.1016/0012-821X(96)00154-9).
- Holland, Paul W., and Roy E. Welsch. 1977. "Robust Regression Using Iteratively Reweighted Least-Squares." *Communications in Statistics - Theory and Methods* 6 (9): 813–27. <https://doi.org/10.1080/03610927708827533>.
- Jacobs, Allison M., Alistair J. Harding, and Graham M. Kent. 2007. "Axial Crustal Structure of the Lau Back-Arc Basin from Velocity Modeling of Multichannel Seismic Data." *Earth and Planetary Science Letters* 259 (3–4): 239–55. <https://doi.org/10.1016/j.epsl.2007.04.021>.

- Jenner, G. A., P. A. Cawood, M. Rautenschlein, and W. M. White. 1987. "Composition of Back-Arc Basin Volcanics, Valu Fa Ridge, Lau Basin: Evidence for a Slab-Derived Component in Their Mantle Source." *Journal of Volcanology and Geothermal Research* 32 (1): 209–22. [https://doi.org/10.1016/0377-0273\(87\)90045-X](https://doi.org/10.1016/0377-0273(87)90045-X).
- Karig, Daniel E. 1970. "Ridges and Basins of the Tonga-Kermadec Island Arc System." *Journal of Geophysical Research* 75 (2): 239–54. <https://doi.org/10.1029/JB075i002p00239>.
- Karson, Jeffrey A. 1998. "Internal Structure of Oceanic Lithosphere: A Perspective from Tectonic Windows." In *Geophysical Monograph Series*, edited by W. Roger Buck, Paul T. Delaney, Jeffrey A. Karson, and Yves Lagabrielle, 177–218. Washington, D. C.: American Geophysical Union. <https://doi.org/10.1029/GM106p0177>.
- Karson, J. A., E. M. Klein, S. D. Hurst, C. E. Lee, P. A. Rivizzigno, D. Curewitz, A. R. Morris, et al. 2002. "Structure of Uppermost Fast-Spread Oceanic Crust Exposed at the Hess Deep Rift: Implications for Subaxial Processes at the East Pacific Rise: STRUCTURE OF FAST-SPREAD OCEANIC CRUST." *Geochemistry, Geophysics, Geosystems* 3 (1): n/a-n/a. <https://doi.org/10.1029/2001GC000155>.
- Kent, Adam J. R., David W. Peate, Sally Newman, Edward M. Stolper, and Julian A. Pearce. 2002. "Chlorine in Submarine Glasses from the Lau Basin: Seawater Contamination and Constraints on the Composition of Slab-Derived Fluids." *Earth and Planetary Science Letters* 202 (2): 361–77. [https://doi.org/10.1016/S0012-821X\(02\)00786-0](https://doi.org/10.1016/S0012-821X(02)00786-0).
- Kenter, Jeroen A.M., and Michael Ivanov. 1995. *Proceedings of the Ocean Drilling Program, 143 Scientific Results*. Edited by E.L. Winterer, W.W. Sager, J.V. Firth, and J.M. Sinton. Vol. 143. Proceedings of the Ocean Drilling Program. Ocean Drilling Program. <https://doi.org/10.2973/odp.proc.sr.143.1995>.
- Kim, Eunyong, Douglas R. Toomey, Emilie E. E. Hooft, William S. D. Wilcock, Robert T. Weekly, Sang-Mook Lee, and Young Hee Kim. 2018. "Upper Crustal  $V_p / V_s$  Ratios at the Endeavour Segment, Juan de Fuca Ridge, from Joint Inversion of  $P$  and  $S$  Travel Times: Implications for Hydrothermal Circulation." *Geochemistry, Geophysics, Geosystems*, December, 2018GC007921. <https://doi.org/10.1029/2018GC007921>.
- Lin, Jian, and Jason Phipps Morgan. 1992. "The Spreading Rate Dependence of Three-Dimensional Mid-Ocean Ridge Gravity Structure." *Geophysical Research Letters* 19 (1): 13–16. <https://doi.org/10.1029/91GL03041>.
- Livermore, Roy, Alex Cunningham, Lieve Vanneste, and Robert Larter. 1997. "Subduction Influence on Magma Supply at the East Scotia Ridge." *Earth and Planetary Science Letters* 150 (3–4): 261–75. [https://doi.org/10.1016/S0012-821X\(97\)00074-5](https://doi.org/10.1016/S0012-821X(97)00074-5).
- Margrave, Gary F. 2000. "New Seismic Modelling Facilities in Matlab" 12: 45.
- Martinez, Fernando, and Brian Taylor. 2002. "Mantle Wedge Control on Back-Arc Crustal Accretion." *Nature* 416 (6879): 417–20. <https://doi.org/10.1038/416417a>.
- Martinez, Fernando, Brian Taylor, Edward T. Baker, Joseph A. Resing, and Sharon L. Walker. 2006. "Opposing Trends in Crustal Thickness and Spreading Rate along the Back-Arc Eastern Lau Spreading Center: Implications for Controls on Ridge Morphology, Faulting, and Hydrothermal Activity." *Earth and Planetary Science Letters* 245 (3–4): 655–72. <https://doi.org/10.1016/j.epsl.2006.03.049>.

- Michael, P. J., S. Escrig, A. Bezos, C. H. Langmuir, R. J. Arculus, and C. I. Goddard. 2011. "Along- and Across-Arc Basalt Geochemical Trends of Seamounts in Lau Basin: Evidence for Fluid Components and Mantle Melting." *AGU Fall Meeting Abstracts* 54 (December): V54B-02.
- Morgan, Jason Phipps, and Y. John Chen. 1993. "The Genesis of Oceanic Crust: Magma Injection, Hydrothermal Circulation, and Crustal Flow." *Journal of Geophysical Research: Solid Earth* 98 (B4): 6283–97. <https://doi.org/10.1029/92JB02650>.
- Morgan, Jason Phipps, and Y. John Ghen. 1993. "Dependence of Ridge-Axis Morphology on Magma Supply and Spreading Rate." *Nature* 364 (6439): 706–8. <https://doi.org/10.1038/364706a0>.
- Nicolas, A. 1989. "The Various Ophiolites and Their Oceanic Environments of Origin." In *Structures of Ophiolites and Dynamics of Oceanic Lithosphere*, edited by A. Nicolas, 187–201. Petrology and Structural Geology. Dordrecht: Springer Netherlands. [https://doi.org/10.1007/978-94-009-2374-4\\_8](https://doi.org/10.1007/978-94-009-2374-4_8).
- Parmentier, E. M., and Jason Phipps Morgant. 1990. "Spreading Rate Dependence of Three-Dimensional Structure in Oceanic Spreading Centres." *Nature* 348 (6299): 325–28. <https://doi.org/10.1038/348325a0>.
- Parson, L. M., J. A. Pearce, B. J. Murton, and R. A. Hodkinson. 1990. "Role of Ridge Jumps and Ridge Propagation in the Tectonic Evolution of the Lau Back-Arc Basin, Southwest Pacific." *Geology* 18 (5): 470. [https://doi.org/10.1130/0091-7613\(1990\)018<0470:RORJAR>2.3.CO;2](https://doi.org/10.1130/0091-7613(1990)018<0470:RORJAR>2.3.CO;2).
- Peacock, S. M., N. I. Christensen, M. G. Bostock, and P. Audet. 2011. "High Pore Pressures and Porosity at 35 Km Depth in the Cascadia Subduction Zone." *Geology* 39 (5): 471–74. <https://doi.org/10.1130/G31649.1>.
- Pearce, Julian A., Michelle Ernewein, Sherman H. Bloomer, Lindsay M. Parson, Bramley J. Murton, and Lynn E. Johnson. 1994. "Geochemistry of Lau Basin Volcanic Rocks: Influence of Ridge Segmentation and Arc Proximity." *Geological Society, London, Special Publications* 81 (1): 53–75. <https://doi.org/10.1144/GSL.SP.1994.081.01.04>.
- Peirce, Christine, Ian M. Turner, and Martin C. Sinha. 2001. "Crustal Structure, Accretionary Processes and Rift Propagation: A Gravity Study of the Intermediate-spreading Valu Fa Ridge, Lau Basin." *Geophysical Journal International* 146 (1): 53–73. <https://doi.org/10.1046/j.0956-540x.2001.01445.x>.
- Perfit, M.R. 2001. "Mid-Ocean Ridge Geochemistry and Petrology." In *Encyclopedia of Ocean Sciences*, 815–25. Elsevier. <https://doi.org/10.1016/B978-012374473-9.00096-5>.
- Püthe, C., and T. Gerya. 2014. "Dependence of Mid-Ocean Ridge Morphology on Spreading Rate in Numerical 3-D Models." *Gondwana Research* 25 (1): 270–83. <https://doi.org/10.1016/j.gr.2013.04.005>.
- Reid, I., and H. R. Jackson. 1981. "Oceanic Spreading Rate and Crustal Thickness." *Marine Geophysical Researches* 5 (2): 165–72. <https://doi.org/10.1007/BF00163477>.
- Rollinson, Hugh. 2017. "Masirah – the Other Oman Ophiolite: A Better Analogue for Mid-Ocean Ridge Processes?" *Geoscience Frontiers* 8 (6): 1253–62. <https://doi.org/10.1016/j.gsf.2017.04.009>.
- Saar, Martin O., and Michael Manga. 1999. "Permeability-Porosity Relationship in Vesicular Basalts." *Geophysical Research Letters* 26 (1): 111–14. <https://doi.org/10.1029/1998GL900256>.

- Shearer, P. M. 1988. “Cracked Media, Poisson’s Ratio and the Structure of the Upper Oceanic Crust.” *Geophysical Journal International* 92 (2): 357–62. <https://doi.org/10.1111/j.1365-246X.1988.tb01149.x>.
- Sisson, T. W., and T. L. Grove. 1992. “Experimental Investigations of the Role of H<sub>2</sub>O in Calc-Alkaline Differentiation and Subduction Zone Magmatism.” *Contributions to Mineralogy and Petrology* 113 (2): 143–66. <https://doi.org/10.1007/BF00283225>.
- Sleeper, Jonathan D., and Fernando Martinez. 2014. “Controls on Segmentation and Morphology along the Back-Arc Eastern Lau Spreading Center and Valu Fa Ridge.” *Journal of Geophysical Research: Solid Earth* 119 (3): 1678–1700. <https://doi.org/10.1002/2013JB010545>.
- Small, Christopher, and David T. Sandwell. 1989. “An Abrupt Change in Ridge Axis Gravity with Spreading Rate.” *Journal of Geophysical Research: Solid Earth* 94 (B12): 17383–92. <https://doi.org/10.1029/JB094iB12p17383>.
- Spudich, Paul, and John Orcutt. 1980. “Petrology and Porosity of an Oceanic Crustal Site: Results from Wave Form Modeling of Seismic Refraction Data.” *Journal of Geophysical Research: Solid Earth* 85 (B3): 1409–33. <https://doi.org/10.1029/JB085iB03p01409>.
- Stern, Robert J., Sherman H. Bloomer, Fernando Martinez, Toshitsugu Yamazaki, and T. Mark Harrison. 1996. “The Composition of Back-Arc Basin Lower Crust and Upper Mantle in the Mariana Trough: A First Report.” *The Island Arc* 5 (3): 354–72. <https://doi.org/10.1111/j.1440-1738.1996.tb00036.x>.
- Stolper, Edward, and Sally Newman. 1994. “The Role of Water in the Petrogenesis of Mariana Trough Magmas.” *Earth and Planetary Science Letters* 121 (3): 293–325. [https://doi.org/10.1016/0012-821X\(94\)90074-4](https://doi.org/10.1016/0012-821X(94)90074-4).
- Taylor, Brian, Kirsten E. Zellmer, Fernando Martinez, and Andrew Goodliffe. 1996. “Sea-Floor Spreading in the Lau Back-Arc Basin.” *EPSL*.
- Thorbecke, Jan W., and Deyan Draganov. 2011. “Finite-Difference Modeling Experiments for Seismic Interferometry.” *GEOPHYSICS* 76 (6): H1–18. <https://doi.org/10.1190/geo2010-0039.1>.
- Turner, Ian M., Christine Peirce, and Martin C. Sinha. 1999. “Seismic Imaging of the Axial Region of the Valu Fa Ridge, Lau Basin—the Accretionary Processes of an Intermediate Back-Arc Spreading Ridge.” *Geophysical Journal International* 138 (2): 495–519. <https://doi.org/10.1046/j.1365-246X.1999.00883.x>.
- Vallier, T.L., G.A. Jenner, F.A. Frey, J.B. Gill, A.S. Davis, A.M. Volpe, J.W. Hawkins, et al. 1991. “Subalkaline Andesite from Valu Fa Ridge, a Back-Arc Spreading Center in Southern Lau Basin: Petrogenesis, Comparative Chemistry, and Tectonic Implications.” *Chemical Geology* 91 (3): 227–56. [https://doi.org/10.1016/0009-2541\(91\)90002-9](https://doi.org/10.1016/0009-2541(91)90002-9).
- Vera, Emilio E., and John B. Diebold. 1994. “Seismic Imaging of Oceanic Layer 2A between 9°30’N and 10°N on the East Pacific Rise from Two-Ship Wide-Aperture Profiles.” *Journal of Geophysical Research: Solid Earth* 99 (B2): 3031–41. <https://doi.org/10.1029/93JB02107>.
- White, R. S., and R. A. Stephen. 1980. “Compressional to Shear Wave Conversion in Oceanic Crust.” *Geophysical Journal International* 63 (2): 547–65. <https://doi.org/10.1111/j.1365-246X.1980.tb02637.x>.

- White, Robert S., Dan McKenzie, and R. Keith O’Nions. 1992. “Oceanic Crustal Thickness from Seismic Measurements and Rare Earth Element Inversions.” *Journal of Geophysical Research: Solid Earth* 97 (B13): 19683–715. <https://doi.org/10.1029/92JB01749>.
- Wiedicke, Michael, and Jenny Collier. 1993. “Morphology of the Valu Fa Spreading Ridge in the Southern Lau Basin.” *Journal of Geophysical Research: Solid Earth* 98 (B7): 11769–82. <https://doi.org/10.1029/93JB00708>.
- Wilcock, William S. D., Sean C. Solomon, G. M. Purdy, and Douglas R. Toomey. 1995. “Seismic Attenuation Structure of the East Pacific Rise near 9°30’N.” *Journal of Geophysical Research: Solid Earth* 100 (B12): 24147–65. <https://doi.org/10.1029/95JB02280>.
- Wilkens, Roy H., Gerard J. Fryer, and Jill Karsten. 1991. “Evolution of Porosity and Seismic Structure of Upper Oceanic Crust: Importance of Aspect Ratios.” *Journal of Geophysical Research: Solid Earth* 96 (B11): 17981–95. <https://doi.org/10.1029/91JB01454>.
- Zellmer, Kirsten E., and Brian Taylor. 2001. “A Three-Plate Kinematic Model for Lau Basin Opening.” *Geochemistry, Geophysics, Geosystems* 2 (5). <https://doi.org/10.1029/2000GC000106>.
- Zoeppritz, K. 1919. *On the Reflection and Propagation of Seismic Waves*. Gottinger Nachrichten.

## Appendix A

### 3-component Ocean Bottom Seismographs (OBS) description and orientation calculation

OBS's used in this study were obtained from the National Ocean Bottom Seismometer Instrument Pool (OBSIP), each containing a hydrophone (High Tech HTI-90-U) and a gimballed 3-component geophone (either a Geospace GS-11D from the Woods Hole Oceanographic Institution (WHOI) pool or a Mark L28 from the Scripps Institution of Oceanography (SIO) pool). The WHOI OBS is a compact case of components in which the sensor (hydrophone and geophone) is decoupled from the electronics and battery package, resulting in low ocean current induced noise on the sensor. The SIO OBS is a frame-mounted device attached to a large anchor. The sensors are placed within the frame, and were found to have recorded instrument-generated noise in some cases.

Both types of geophones were gimballed in nature, i.e. the vertical component remained upright during its descent to the seafloor while the orientation of horizontal components was unknown. We used water wave polarisation analysis to find the orientation of horizontal components of the OBS. We picked the direct water wave first breaks on record sections of the hydrophone channel and studied the particle motions of waves coming from within 3 km range from the station (as shown in **Figure A1**). We selected a window of 0.1-0.15s behind first water wave break and rotated the 2 horizontal components (H1 and H2) into N-E reference frame followed by another rotation to orient them in radial direction with respect to each source using the following equation,

$$\begin{bmatrix} R \\ T \end{bmatrix} = \begin{bmatrix} \cos(\theta_a) & -\sin(\theta_a) \\ \sin(\theta_a) & \cos(\theta_a) \end{bmatrix} \begin{bmatrix} \cos(\theta_b) & -\sin(\theta_b) \\ \sin(\theta_b) & \cos(\theta_b) \end{bmatrix} \begin{bmatrix} H1 \\ H2 \end{bmatrix} \quad (\text{A1})$$

where  $\theta_a$  is the orientation of H1 from north and  $\theta_b$  is the azimuth of source with respect to the receiver. We obtained 2 supplementary angles which maximises the R/T ratio and we selected the value of  $\theta_a$  which resulted in same polarisation of water wave in radial and vertical component.

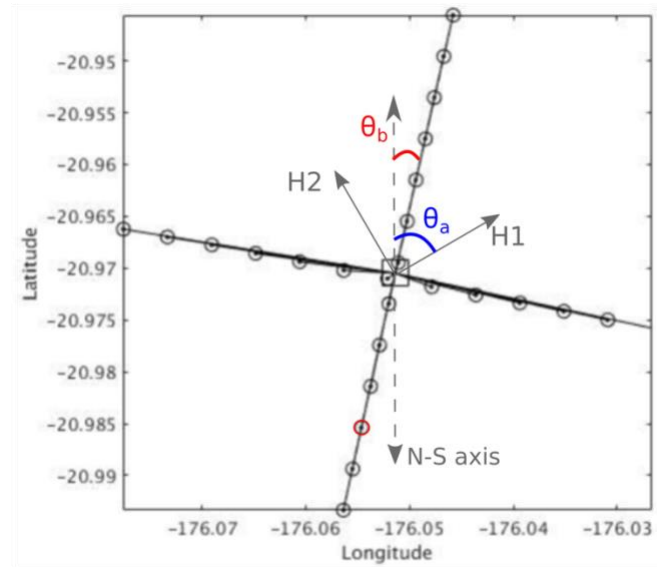


**Figure A1.** Source receiver geometry used for component orientation calculation. Position of receiver (square box) and sources around the receiver (circles) used for the polarisation analysis and horizontal

component (H1 and H2) orientation calculation. Angles  $\theta_a$  (blue) and  $\theta_b$  (red) are defined as source azimuth and receiver orientation respectively.

An example of data collected from the source-receiver geometry (shown in **Figure A1**) is shown in **Figure A2** in unrotated Z-H1-H2 reference frame and rotated Z-R-T reference frame. We can see that post rotation, energy in transverse component is significantly reduced and the polarisations of water wave in vertical (Z) and radial (R) is same.

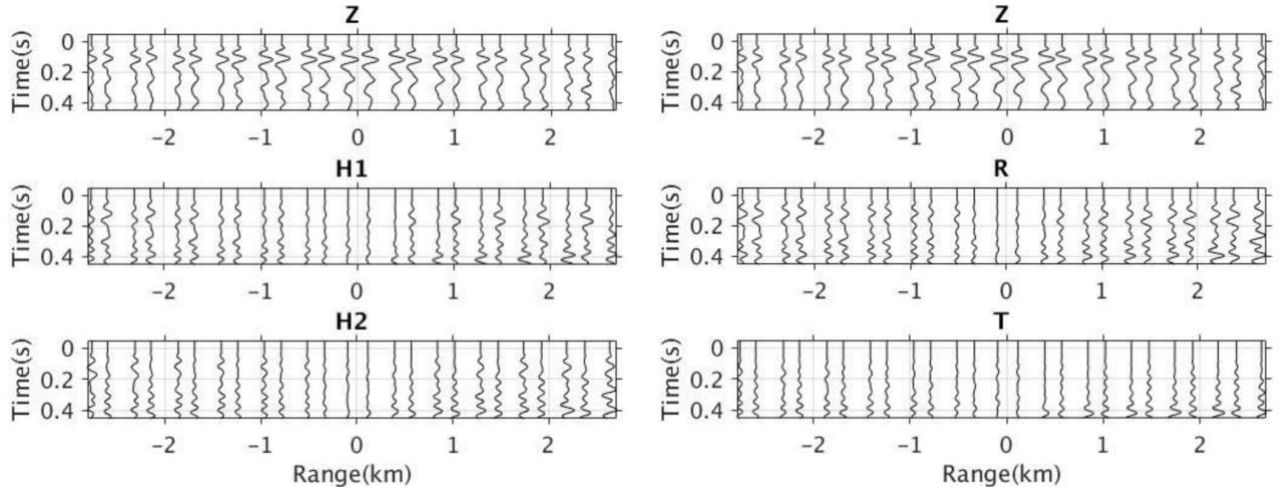


**Figure A2.** Example of common receiver gather recorded in the three components of geophone for the source receiver geometry in **Figure A1**. The time starts from the picked water wave first break. **Left:** Data is recorded by unrotated 3-component geophone in vertical (top) and two perpendicular horizontal directions (H1 and H2). **Right:** Data observed post component rotation in vertical (top) and radial (R) and Transverse (T) direction.

A table summarising the information about all the receivers across the study area is given **Table A1**. The orientation angle of ‘X’ component of each receiver from North, and details about the discarded receivers is given. ‘Status’ column indicates receivers condition: with ‘x’ for discarded and ‘✓’ for good receivers. The reason for discarding a receiver is mentioned in ‘Comment’ column. Receivers discarded with no comments were found to have poor signal-to-noise ratio due to ground coupling, instrument noise etc.

**Table A1.** List of station deployment numbers, latitude and longitude, water depth, orientation of H1 component from North and comments about the OBS.

Dep	Type	Longitude	Latitude	Water Depth(m)	Status	Orientation of X from North	Horizontal Sensor flip	Comment
1	W	-176.051	-20.970	2393	✓	187	1	
2	W	-176.035	-20.897	2405	✓	184	1	
3	W	-176.019	-20.822	2319	x	-	-	
4	W	-175.985	-20.752	2288	✓	235	0	
5	S	-175.987	-20.675	2277	✓	211.5	1	
6	S	-175.963	-20.601	2286	✓	195	1	
7	S	-175.956	-20.527	2238	✓	158	1	
8	S	-175.940	-20.453	2288	✓	-2	1	
9	S	-176.007	-20.402	2430	✓	-32	1	
10	S	-176.079	-20.427	2444	✓	110	1	
11	S	-176.023	-20.476	2399	✓	26	1	
12	S	-176.086	-20.502	2432	✓	86	1	
13	S	-176.038	-20.550	2331	x	-	-	Dead H2
14	S	-176.103	-20.575	2438	x	-	-	
15	S	-176.054	-20.623	2301	✓	234	1	
16	S	-176.120	-20.648	2419	✓	207	1	
17	W	-176.071	-20.696	2280	✓	132	1	
18	W	-176.139	-20.721	2346	x	-	-	
19	W	-176.089	-20.769	2288	x	-	-	
20	W	-176.155	-20.791	2217	x	-	-	Dead H1, Low gain H2
21	W	-176.102	-20.845	2386	x	-	-	
22	W	-176.177	-20.870	2093	✓	135	1	
23		0.000	0.000	0		0	1	Dead
24	S	-176.198	-20.943	2207	✓	60	1	
25	W	-176.222	-20.900	2231	✓	70	1	
26	W	-176.280	-20.928	2408	x	-	-	Dead H2
27	W	-176.263	-20.854	2477	✓	-52	1	
28	W	-176.205	-20.826	2095	x	-	-	
29	W	-176.244	-20.780	2335	✓	0	0	
30	W	-176.186	-20.752	2113	x	-	-	
31	S	-176.227	-20.706	2482	✓	167	1	
32	S	-176.174	-20.676	2207	✓	-62	1	
33	S	-176.170	-20.637	2406	✓	311	-	
34	S	-176.214	-20.631	2583	✓	188.55	1	
35	S	-176.159	-20.603	2500	x	-	-	
36	S	-176.152	-20.566	2521	✓	102	1	
37	S	-176.199	-20.558	2539	✓	220	1	

38	S	-176.143	-20.530	2512	✓	120	1	
39	S	-176.180	-20.485	2719	✓	25	1	
40	S	-176.173	-20.448	2657	✓	170	1	
41	S	-176.127	-20.457	2408	✓	-2	0	
42	S	-176.164	-20.411	2688	✓	247	1	
43	S	-176.109	-20.381	2362	✓	136	1	
44	S	-176.212	-20.362	2379	x	-	-	Dead H2
45	S	-176.228	-20.435	2338	✓	280	1	
46	W	-176.246	-20.509	2371	✓	134	1	
47	W	-176.262	-20.583	2263	✓	180	1	
48	W	-176.278	-20.658	2375	x	-	-	
49	W	-176.294	-20.732	2368	✓	170	-	
50	W	-176.310	-20.806	2427	✓	35	1	
51	S	-176.324	-20.881	2248	x	-	-	Partially flooded
52	S	-176.410	-20.903	2397	✓	240	1	
53	S	-176.393	-20.830	2399	✓	25	1	
54	S	-176.377	-20.757	2338	✓	33	1	
55	S	-176.361	-20.683	2243	x	-	-	Dead
56	S	-176.345	-20.608	2302	x	-	-	Dead H2
57	S	-176.329	-20.529	2040	✓	98	1	
58	S	-176.312	-20.453	2257	✓	110	1	
59	S	-176.297	-20.383	2454	✓	78	1	
60	W	-176.298	-20.307	2294	✓	308	1	
61	W	-176.293	-20.231	2373	x	-	-	
62	W	-176.278	-20.163	2594	x	-	-	
63	W	-176.261	-20.082	2610	✓	14	1	
64	W	-176.193	-20.133	2464	x	-	-	Low gain H1 H2
65	W	-176.208	-20.207	2492	✓	13	1	
66	S	-176.225	-20.280	2304	✓	35	1	
67	S	-176.167	-20.330	2365	x	-	-	
68	S	-176.122	-20.301	2711	✓	106	1	
69	S	-176.160	-20.255	2380	✓	195	1	
70	S	-176.107	-20.227	2751	✓	260	1	
71	S	-176.144	-20.180	2571	✓	31	1	
72	S	-176.128	-20.107	2702	✓	90	1	
73	S	-176.089	-20.154	2683	x	-	-	
74	W	-176.036	-20.124	2500	x	-	-	
75	W	-175.981	-20.176	2337	✓	-30	1	
76	W	-176.048	-20.201	2378	✓	17	1	
77	W	-175.997	-20.249	2418	x	-	-	
78	W	-176.070	-20.274	2430	✓	172	1	
79	W	-176.083	-20.348	2383	x	-	-	

80	W	-176.017	-20.321	2404	x	-	-	Dead H2
81	W	-175.950	-20.372	2121	x	-	-	Dead H2
82	W	-175.943	-20.292	2141	x	-	-	
83	W	-175.918	-20.223	2191	x	-	-	Dead H1
84	W	-175.903	-20.151	2242	✓	104	1	

## Appendix B

This Appendix illustrates the processing steps applied to the seismic data. Some pre-processing steps are not discussed here, for which the reader is referred to Dunn et al. (2013). After OBS horizontal components orientation was known using the method explained in **Appendix A** (e.g., X-Y in **Figure B2**), the X-Y components were rotated about Z to get R-T components with respect to each source ( $R_1$  and  $R_2$  for sources  $S_1$  and  $S_2$  respectively in **Figure B2**). The second rotation is made about the transverse axis to maximise the amplitude of incoming crustal P-wave refractions on the L-component, schematically shown in **Figure B2**, for a head wave generated by source S. The second rotation about the transverse axis is only used to analyse crustal refractions and phase converted arrivals. Complete implementation of the workflow on 3-component OBS data is shown in **Figure B3**.

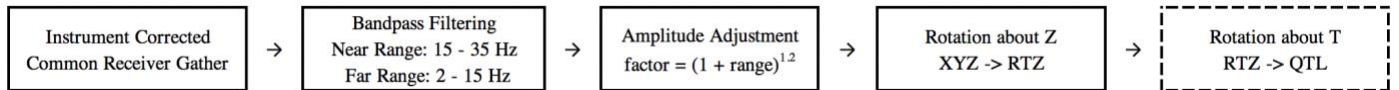


**Figure B1.** Data processing flow chart. Steps in solid boxes were implemented on all the data. The step in dashed box was implemented only in far range data.

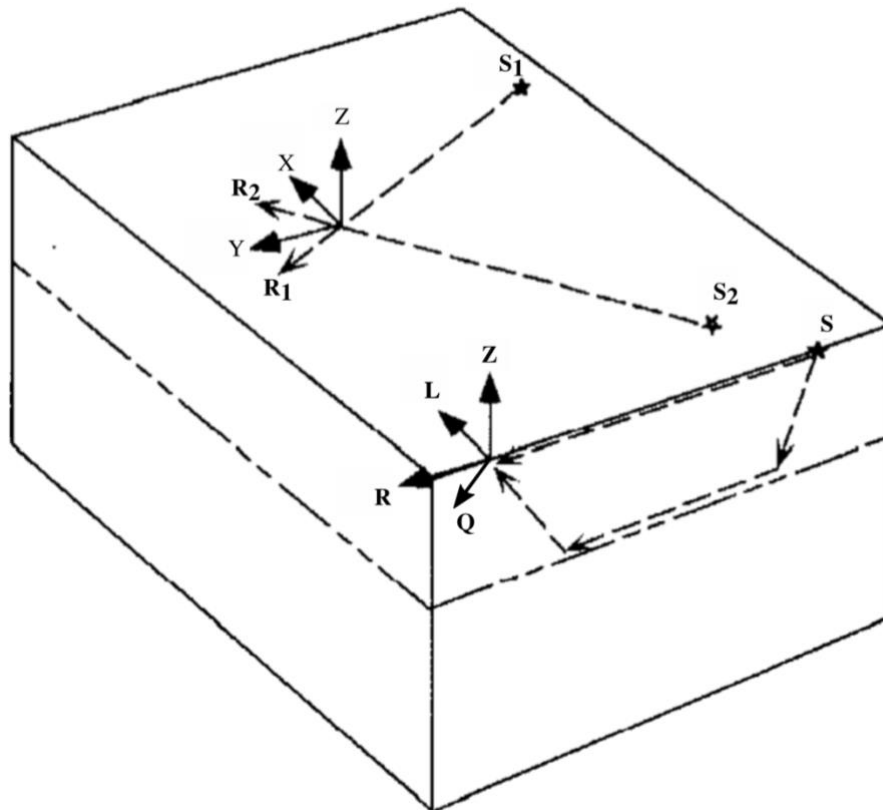


**Figure B2.** Cartoon showing component rotation. First step of rotation from X-Y-Z to R-T-Z with respect to each source is schematically represented in the top face of cube for sources  $S_1$  and  $S_2$ . Second rotation from R-T-Z to Q-L-T is represented at the edge of the cube with respect to a head wave from source S. (After Guevara and Stewart, 1988)

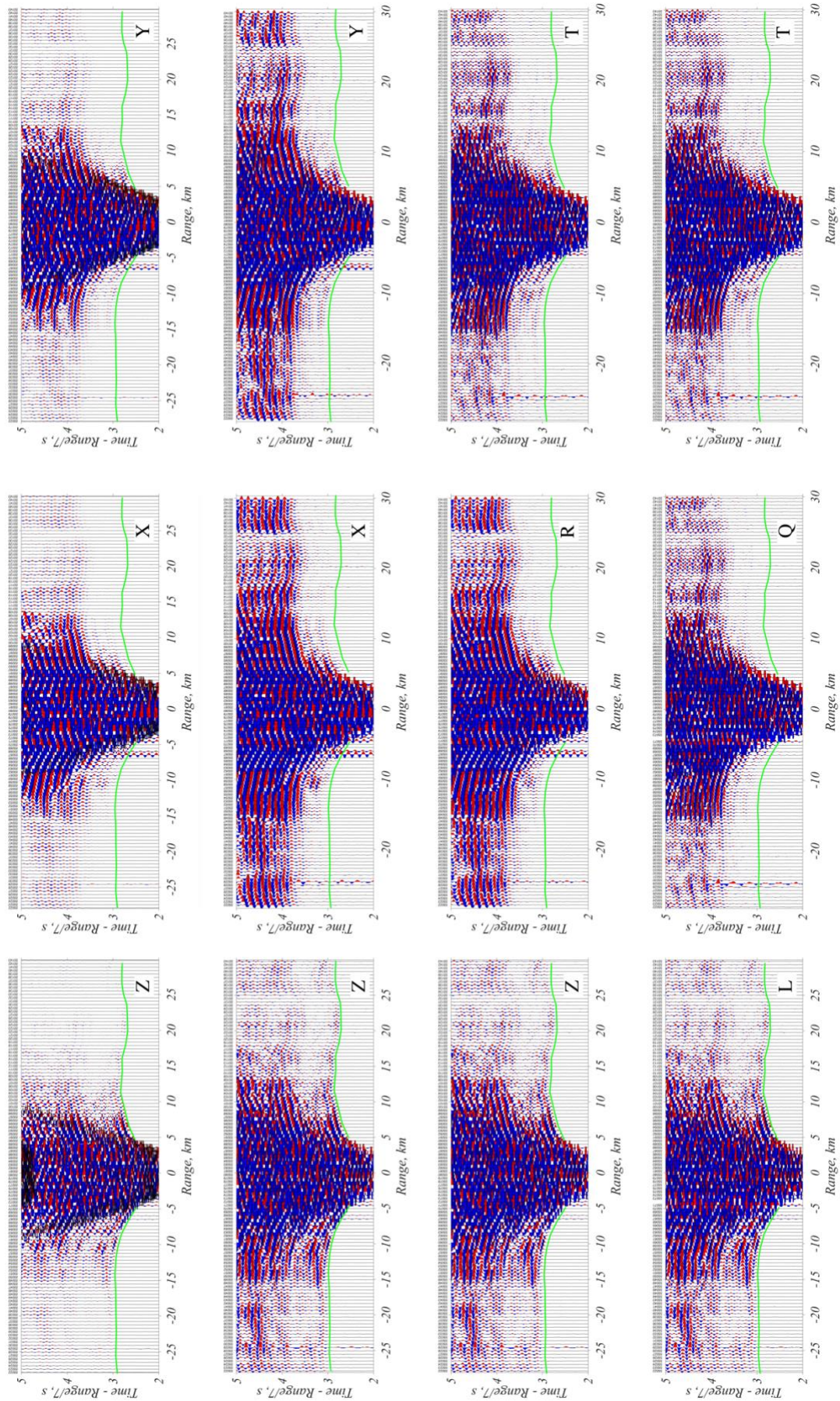


**Figure B3.** Seismic data processing flow demonstrated in OBS data. 1) Instrument response corrected common receiver gather recorded in the 3 perpendicular directions with observed Pg refraction marked in green line for reference. 2) Bandpass filtered (5-15Hz) and amplitude adjusted CRG. 3) Radial (R) and Transverse (T) direction traces with respect to each source obtained by X-Y components rotation about Z. 4) L and Q components obtained by Z-R components rotation about T by a constant angle of  $12^\circ$ . Notice the reduced amplitude of crustal P-wave refractions in Q as compared to R.

## Appendix C

In this appendix, we describe the numerical scheme used to simulate elastic wave propagation through isotropic media using difference equations accurate to 4<sup>th</sup> order in space and 2<sup>nd</sup> order in time (Levander 1988). The linearized equation of motion (Newton's second law) and equation of deformation (Hook's law) is given by:

$$\begin{aligned} \frac{\partial V_x}{\partial t} &= \frac{-1}{\rho} \left( \frac{\partial \sigma_{xx}}{\partial x} + \frac{\partial \sigma_{xz}}{\partial z} \right); & \frac{\partial V_z}{\partial t} &= \frac{-1}{\rho} \left( \frac{\partial \sigma_{zz}}{\partial z} + \frac{\partial \sigma_{xz}}{\partial x} \right) \\ \frac{\partial \sigma_{xx}}{\partial t} &= - \left( \frac{1}{\kappa} \frac{\partial V_x}{\partial x} + \lambda \frac{\partial V_z}{\partial z} \right); & \frac{\partial \sigma_{zz}}{\partial t} &= - \left( \frac{1}{\kappa} \frac{\partial V_z}{\partial z} + \lambda \frac{\partial V_x}{\partial x} \right); & \frac{\partial \sigma_{xz}}{\partial t} &= -\mu \left( \frac{\partial V_z}{\partial x} + \frac{\partial V_x}{\partial z} \right) \end{aligned} \quad (C1)$$

where the parameters are defined as:

$V_x, V_z$  : Horizontal and Vertical Velocity

$\sigma_{xx}, \sigma_{zz}$  : Compressional Stress

$\sigma_{xz}$  : Shear Stress

$\rho$  : Density

$\kappa$  : Bulk Modulus

$\lambda, \mu$  : Lamé's Parameters (Note:  $\lambda + 2\mu / 3 = \kappa$ )

$$\sigma_p = \frac{1}{1 + \frac{\lambda}{\lambda + 2\mu}} * (\sigma_{xx} + \sigma_{zz})$$

The partial differential equations are discretised using a centred finite difference approach, with medium properties defined in staggered grid fashion as shown in **Figure C1**. The explicit scheme first updates velocities at half time steps from  $k-1/2$  to  $k+1/2$  given by:

$$\begin{aligned} V_x^{k+1/2}_{(i-1/2,j)} &= V_x^{k-1/2}_{(i-1/2,j)} - S * b_{(i-1/2,j)} \left( c1 \left( \sigma_{xx}^k_{(i,j)} - \sigma_{xx}^k_{(i-1,j)} + \sigma_{xz}^k_{(i,j+1)} - \sigma_{xz}^k_{(i,j)} \right) + c2 \left( \sigma_{xx}^k_{(i+1,j)} - \sigma_{xx}^k_{(i-2,j)} + \sigma_{xz}^k_{(i,j+2)} - \sigma_{xz}^k_{(i,j-1)} \right) \right) \\ V_z^{k+1/2}_{(i,j-1/2)} &= V_z^{k-1/2}_{(i,j-1/2)} - S * b_{(i,j-1/2)} \left( c1 \left( \sigma_{zz}^k_{(i,j)} - \sigma_{zz}^k_{(i,j-1)} + \sigma_{xz}^k_{(i+1,j)} - \sigma_{xz}^k_{(i,j)} \right) + c2 \left( \sigma_{zz}^k_{(i,j+1)} - \sigma_{zz}^k_{(i,j-2)} + \sigma_{xz}^k_{(i+2,j)} - \sigma_{xz}^k_{(i-1,j)} \right) \right) \end{aligned} \quad (C2)$$

where  $S = dt/dx$ ,  $b$  is buoyancy ( $= 1/\rho$ ),  $c1$  and  $c2$  are the inner and outer difference coefficients for the fourth-order approximation to the first derivative,  $9/8$  and  $-1/24$ , respectively. P wave was decomposed from discretised compressional stress ( $\sigma_p$ ) given by:

$$\begin{aligned} Vp_x^{k+1/2}_{(i-1/2,j)} &= Vp_x^{k-1/2}_{(i-1/2,j)} - S * b_{(i-1/2,j)} \left( c1 \left( \sigma_p^k_{(i,j)} - \sigma_p^k_{(i-1,j)} \right) + c2 \left( \sigma_p^k_{(i+1,j)} - \sigma_p^k_{(i-2,j)} \right) \right) \\ Vp_z^{k+1/2}_{(i,j-1/2)} &= Vp_z^{k-1/2}_{(i,j-1/2)} - S * b_{(i,j-1/2)} \left( c1 \left( \sigma_p^k_{(i,j)} - \sigma_p^k_{(i,j-1)} \right) + c2 \left( \sigma_p^k_{(i,j+1)} - \sigma_p^k_{(i,j-2)} \right) \right) \end{aligned} \quad (C3)$$

Next, the scheme updates stresses from time step  $k$  to  $k+1$  given by:

$$\begin{aligned} \sigma_{xx}^{k+1}_{i,j} &= \sigma_{xx}^k_{i,j} - S \left( c1 \left( l2m_{i,j} * \left( V_x^{k+1/2}_{(i+1/2,j)} - V_x^{k+1/2}_{(i-1/2,j)} \right) + \lambda_{i,j} * \left( V_z^{k+1/2}_{(i,j+1/2)} - V_z^{k+1/2}_{(i,j-1/2)} \right) \right) + c2 \left( l2m_{i,j} * \left( V_x^{k+1/2}_{(i+3/2,j)} - V_x^{k+1/2}_{(i-3/2,j)} \right) + \lambda_{i,j} * \left( V_z^{k+1/2}_{(i,j+3/2)} - V_z^{k+1/2}_{(i,j-3/2)} \right) \right) \right) \\ \sigma_{zz}^{k+1}_{i,j} &= \sigma_{zz}^k_{i,j} - S \left( c1 \left( l2m_{i,j} * \left( V_z^{k+1/2}_{(i,j+1/2)} - V_z^{k+1/2}_{(i,j-1/2)} \right) + \lambda_{i,j} * \left( V_x^{k+1/2}_{(i+1/2,j)} - V_x^{k+1/2}_{(i-1/2,j)} \right) \right) + c2 \left( l2m_{i,j} * \left( V_z^{k+1/2}_{(i,j+3/2)} - V_z^{k+1/2}_{(i,j-3/2)} \right) + \lambda_{i,j} * \left( V_x^{k+1/2}_{(i+3/2,j)} - V_x^{k+1/2}_{(i-3/2,j)} \right) \right) \right) \\ \sigma_{xz}^{k+1}_{i+1/2,j+1/2} &= \sigma_{xz}^k_{i+1/2,j+1/2} - S * \mu_{i+1/2,j+1/2} \left( c1 \left( \left( V_z^{k+1/2}_{(i+1/2,j)} - V_z^{k+1/2}_{(i-1/2,j)} \right) + \left( V_x^{k+1/2}_{(i,j+1/2)} - V_x^{k+1/2}_{(i,j-1/2)} \right) \right) + c2 \left( \left( V_z^{k+1/2}_{(i+3/2,j)} - V_z^{k+1/2}_{(i-3/2,j)} \right) + \left( V_x^{k+1/2}_{(i,j+3/2)} - V_x^{k+1/2}_{(i,j-3/2)} \right) \right) \right) \end{aligned} \quad (C4)$$

where  $l2m$  is defined as  $(\lambda + 2\mu)$ .

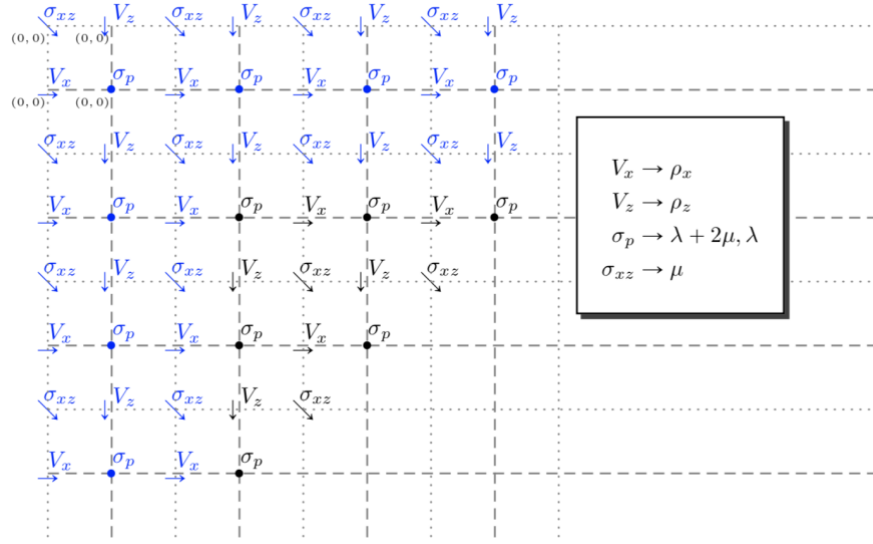


**Figure C1.** Staggered gridding used for numerical calculation of elastic wave propagation in isotropic media for a fourth-order scheme in space (After Thorbecke and Draganov, 2012).  $V_z$ ,  $V_x$  represent the particle velocity of the wavefield in the  $z$  and  $x$  direction, respectively, and  $\sigma_p$  ( $\sigma_{xx}$  or  $\sigma_{zz}$ ),  $\sigma_{xz}$  represent the compressional and shear stress fields respectively. The blue fields are auxiliary points used to calculate the black field values, which are not updated and initialized to zero.

The condition imposed on grid spacing in time ( $\Delta t$ ) and space ( $\Delta x$ ,  $\Delta z$ ) requires :

$$\Delta t \leq \frac{1}{\sqrt{2}} \frac{\min(\Delta x, \Delta z)}{v_{\max}} \quad (C5)$$

The unsuitable choice of time and spatial steps may cause severe dispersion and wave distortion in wave simulation. In order to suppress numerical dispersion, it is usually required that there are 20 sampling points per wavelength:

$$\min(\Delta x, \Delta z) < \frac{v_{\min}}{20 f_{\max}} \quad (C6)$$

For the same frequency, the numerical dispersion increases as the spatial steps increase. However, the dispersion can be depressed if the higher point approximation schemes are used. Time and space steps were governed by equations C5 and C6. The ricker source was set at 10 Hz dominant frequency with a radially decaying cosine taper. The boundaries were padded with zeros throughout the simulation with a taper of 30% to minimise reflections from edges of model.

## Appendix D

**Table D1.** Near surface shear wave velocities and layer thicknesses.

Depl.	Two-way traveltime (SS-phase)	Thickness (H), km	P-wave velocity (Vp), km/s	S-wave velocity (Vs), km/s
1	0.50	0.11	1.7	0.45
3	0.25	0.06	1.7	0.5
4	0.45	0.08	1.6	0.36
5	0.45	0.09	1.6	0.4
6	0.10	0.03	1.7	0.6
7	0.70	0.14	1.7	0.61
8	0.32	0.05	1.6	0.3
9	0.80	0.14	1.6	0.4
10	0.45	0.09	1.6	0.44
11	1.00	0.14	1.6	0.4
12	0.80	0.20	2.2	0.7
15	0.50	0.10	1.6	0.42
16	0.40	0.11	2.2	0.7
17	0.35	0.07	1.6	0.41
22	0.40	0.10	1.7	0.5
24	0.50	0.11	1.7	0.5
27	0.30	0.08	1.7	0.52
31	0.16	0.05	2.0	0.7
33	0.16	0.05	2.0	0.61
34	0.14	0.04	2.0	0.7
37	0.12	0.03	2.0	0.74
38	0.16	0.05	2.0	0.7
39	0.10	0.03	2.0	0.71
40	0.14	0.04	2.0	0.72
41	0.10	0.03	2.0	0.7
42	0.12	0.03	2.0	0.73
43	0.11	0.03	2.2	0.7
44	0.18	0.06	2.0	0.71
45	0.15	0.05	2.0	0.7
46	0.14	0.05	1.9	0.65
47	0.10	0.03	1.9	0.65
49	0.18	0.05	1.9	0.6
50	0.23	0.08	2.0	0.72
52	0.30	0.08	1.6	0.5
53	0.35	0.07	1.6	0.42
54	0.10	0.03	1.8	0.6
57	0.30	0.09	1.9	0.61

58	0.08	0.03	2.0	0.7
59	0.20	0.07	2.0	0.72
60	0.22	0.08	2.2	0.7
63	0.30	0.06	1.7	0.4
65	0.20	0.07	2.0	0.66
66	0.20	0.07	2.0	0.67
69	0.15	0.05	2.2	0.7
70	0.18	0.05	2.2	0.73
75	0.20	0.07	2.1	0.73
76	0.10	0.04	2.1	0.7
78	0.25	0.09	2.1	0.71
84	0.35	0.08	1.7	0.45

## Appendix E

**Table E1.** Layer 2A shear wave velocities and layer thicknesses.

Depl.	Thickness, km	P-wave velocity, km/s	S-wave velocity, km/s	Vp/Vs
1	0.66	2.83	0.87	3.22
2	0.67	2.80	0.82	3.42
3	0.58	2.84	0.96	2.92
4	0.65	2.79	0.90	3.12
6	0.66	2.73	0.92	2.93
8	0.65	2.74	0.90	3.10
9	0.65	2.84	0.91	3.07
11	0.64	2.84	0.84	3.33
12	0.61	2.65	0.91	2.97
16	0.54	2.67	0.91	2.95
24	0.59	2.70	0.93	2.91
27	0.53	2.65	1.09	2.48
33	0.53	2.73	1.02	2.65
34	0.62	3.06	1.19	2.53
38	0.56	2.71	0.97	2.79
39	0.47	2.97	1.10	2.45
42	0.55	2.99	1.20	2.33
43	0.56	2.75	0.90	2.99
47	0.54	2.80	1.17	2.39
49	0.51	2.74	1.19	2.36
50	0.59	2.76	0.92	3.04
52	0.72	2.74	0.94	2.97
53	0.65	2.83	0.90	3.10
54	0.70	2.83	1.08	2.60
58	0.63	2.91	1.04	2.73
59	0.53	2.82	0.96	2.97
60	0.49	2.96	0.96	3.03
63	0.50	3.00	1.27	2.28
65	0.60	2.96	1.20	2.50
66	0.60	2.96	1.25	2.40
69	0.44	2.96	1.21	2.47
71	0.45	3.03	1.29	2.33
72	0.49	3.03	1.70	1.76
76	0.57	2.93	1.27	2.29
78	0.52	2.91	1.11	2.61
84	0.55	2.65	0.96	2.82